Multifunctional Composite Scaffold with Nano-silver, Graphene Oxide, and Macrophage Membrane Vesicles for Sequential Treatment of Infected Bone Defects

Mingjie Sun, Yang Lu, Hongrui Zhang, Weiqian Jiang, Wenzhao Wang, Xiao Huang, Shichun Zhang, Dulei Xiang, Boyu Tang, Yu Chen, Tingmei Chen, Chengjie Lian, and Jian Zhang**

M. Sun, H. Zhang, X. Huang, D. Xiang, B. Tang, Y. Chen, C. Lian, J. Zhang

Department of Orthopedics, the First Affiliated Hospital of Chongqing Medical University, Chongqing 400016, China.

E-mail: zhangjian@hospital.cqmu.edu.cn; lianchj@hospital.cqmu.edu.cn

Y. Lu

Center for Human Tissues and Organs Degeneration, Shenzhen Institute of Advanced Technology, Chinese Academy of Sciences, Shenzhen 518055, China.

W. Jiang, S. Zhang

Department of Orthopedics, the Second Affiliated Hospital of Chongqing Medical University, Chongqing 401336, China.

W. Wang

This article has been accepted for publication and undergone full peer review but has not been through the copyediting, typesetting, pagination and proofreading process, which may lead to differences between this version and the Version of Record. Please cite this article as doi: 10.1002/adhm.202400346.

Department of Orthopedics, Qilu Hospital, Cheeloo College of Medicine, Shandong University, Jinan 250012, China.

T. Chen

Key Laboratory of Clinical Laboratory Diagnostics (Ministry of Education), College of Laboratory Medicine, Chongqing Medical University, Chongqing 400016, China.

Keywords: infected bone defect, silver nanoparticles, graphene oxide, membrane vesicles, immunoregulation

The management of infected bone defects poses a significant clinical challenge, and current treatment modalities exhibit various limitations. This study focuses on the development of a multifunctional composite scaffold comprising nanohydroxyapatite/polyethyleneglycol diacrylate (HP) matrix, silver nanoparticles (AgNPs), graphene oxide (GO), sodium alginate (SA), and M2-type macrophage membrane vesicles (MVs) to enhance the healing of infected bone defects. The composite scaffold demonstrates several key features: first, it releases sufficient quantities of silver ions to effectively eliminate bacteria; second, the controlled release of MVs leads to a notable increase in M2-type macrophages, thereby significantly mitigating the inflammatory response. Additionally, GO acts synergistically with nHA to enhance osteoinductive activity, thereby fostering bone regeneration. Through meticulous *in vitro* and *in vivo* investigations, the composite scaffold exhibits broad-spectrum antimicrobial effects, robust immunomodulatory capabilities, and enhanced osteoinductive activity. This multifaceted composite scaffold presents a promising approach for the sequential treatment of infected bone defects, addressing the antimicrobial,

immunomodulatory, and osteogenic aspects. This study introduces innovative perspectives and offers new and effective treatment alternatives for managing infected bone defects.

1. Introduction

Infected bone defects caused by trauma, surgery, or other factors present major challenges for orthopedic surgeons.[1] Currently, the treatment of infected bone defects relies on traditional surgery and broad-spectrum antibiotics. However, patients are often subjected to the side effects of antibiotics and are at a risk of secondary surgical bone grafting. In addition, bone donors required for bone grafting suffer from scarce sources, size mismatch, and immune rejection.[2, 3] To address these limitations, three-dimensional (3D)-printed scaffolds have attracted much attention in the field of bone tissue engineering because of their personalized customization and high precision.[4, 5] Bone tissue regenerative repair is a complex process,[6] and the presence of infection makes repair even more difficult. Although 3D-printed scaffolds can solve the problems of implant source and matching, 3D-printed scaffolds alone can only provide basic mechanical support and do not exert osteoinductive activity. Therefore, there is a pressing demand for an innovative therapeutic strategy that surpasses the constraints of the current treatment paradigms and can effectively manage infections, orchestrate immune modulation, and foster osteogenesis.

Nanoscale silver particles (AgNPs) exhibit potent antimicrobial activity.[7-9] Unlike antibiotics, AgNPs release silver ions that have antimicrobial effects. Silver ions can disrupt the bacterial cell wall by increasing the membrane permeability of bacteria by aggregating within the inner membrane of the bacteria and interacting with sulfur-containing proteins in the bacterial cell wall.[10, 11] In addition, AgNPs interact with sulfur or phosphorus groups after entering bacteria, causing denaturation of bacterial DNA and proteins, which in turn activates apoptotic pathways and generates reactive oxygen species (ROS) and free radicals.[12, 13] This antibacterial mechanism of AgNPs not only provides a broad-spectrum antimicrobial effect, but also makes it less likely to develop drug resistance. However, AgNPs can penetrate the cell membrane and cause toxicity in human cells. Cytotoxicity is dose-dependent on the concentration of AgNPs.[14, 15]

Immunomodulation plays an important role in bone tissue regeneration and repair.[16] Macrophages are critical effector cells in the immune response and are capable of initiating and mediating host immune responses. Typically, macrophages select the classical M1 phenotype to promote

inflammatory responses or strategically polarize to the pro-healing M2 phenotype. Infection, an important factor in the immune response, causes macrophages to polarize in favor of the M1 phenotype to remove foreign bodies and surrounding necrotic tissue.[17-20] However, a sustained proinflammatory microenvironment affects subsequent bone tissue regeneration. It has been shown that modulating macrophage polarization toward the M2 phenotype is beneficial for reducing local tissue inflammation and creating a favorable bone immune environment.[21-23] It has also been shown that under specific conditions, M2 macrophages can induce the transformation of M1 macrophages into the M2 phenotype, thereby modulating the immune environment.[24, 25] The artificially synthesized M2 phenotype macrophage membrane nano-vesicles (MVs) are more stable and controllable than the direct application of M2 phenotype macrophages. In addition, artificially fabricated MVs have better immune evasion capabilities and can be carefully engineered to reduce interference with the immune system. Sodium alginate is a natural polysaccharide with excellent biocompatibility and does not trigger significant immune responses or cytotoxicity.[26, 27] In addition, sodium alginate can be used to control the release of drugs or bioactive compounds by constructing a sustained-release system, which is crucial for temporal regulation of drug release and long-term therapy.

Graphene oxide (GO), an oxidized derivative of graphene, has attracted much attention in the field of materials science and biomedicine because of its remarkable electrical, mechanical, and thermal conductivity, as well as excellent biocompatibility and bioactivity.[28-30] In addition, the abundance of oxygen-containing functional groups and large specific surface area make GO an effective drug delivery carrier.[31, 32] It has been shown that inoculation of mesenchymal stem cells (MSCs) on GO-coated surfaces accelerates their osteogenic differentiation.[33] GO induces robust osteogenesis independently, overcoming the limitation of additional use of osteogenic growth factors in bone tissue engineering. However, the molecular mechanisms associated with GO promoting osteogenic differentiation of MSCs are unclear. For successful clinical translation of nanomaterials, we need a deeper understanding of nanomaterial-cell interactions.

In this study, we fabricated a 3D-printed composite scaffold by mixing AgNPs and GO with nanohydroxyapatite/polyethylene glycol diacrylate (AGHP) at a suitable ratio. Subsequently, we successfully constructed a multi-effect integrated composite scaffold by filling sodium alginate hydrogel containing M2-type macrophage membrane vesicles inside the scaffold (AGHP@AMVs). Bacterial growth was effectively inhibited by the release of silver ions through pre-existing AgNPs.

With a change in pH around the infected bone defect, MVs in the sodium alginate hydrogel were effectively released, significantly improving the inflammatory response by remodeling the M2 phenotype of macrophages. In addition, the associated cytokines released by M2-type macrophages promoted the migration of MSCs. The large specific surface area of GO further enhanced the colonization of MSCs and synergized with the nanohydroxyapatite (nHA) in the scaffold to exert osteoinductive activity. *In vitro* and *in vivo* studies demonstrated that the composite scaffolds possess satisfactory antimicrobial, immunomodulatory, and osteogenic properties (**Scheme** 1). In addition, high-throughput sequencing revealed a potential mechanism by which GO promotes osteogenic differentiation. Overall, this multi-effect integrated biomaterial scaffold with bone immunomodulatory functions is expected to be a new strategy for the sequential treatment of infected bone defects.

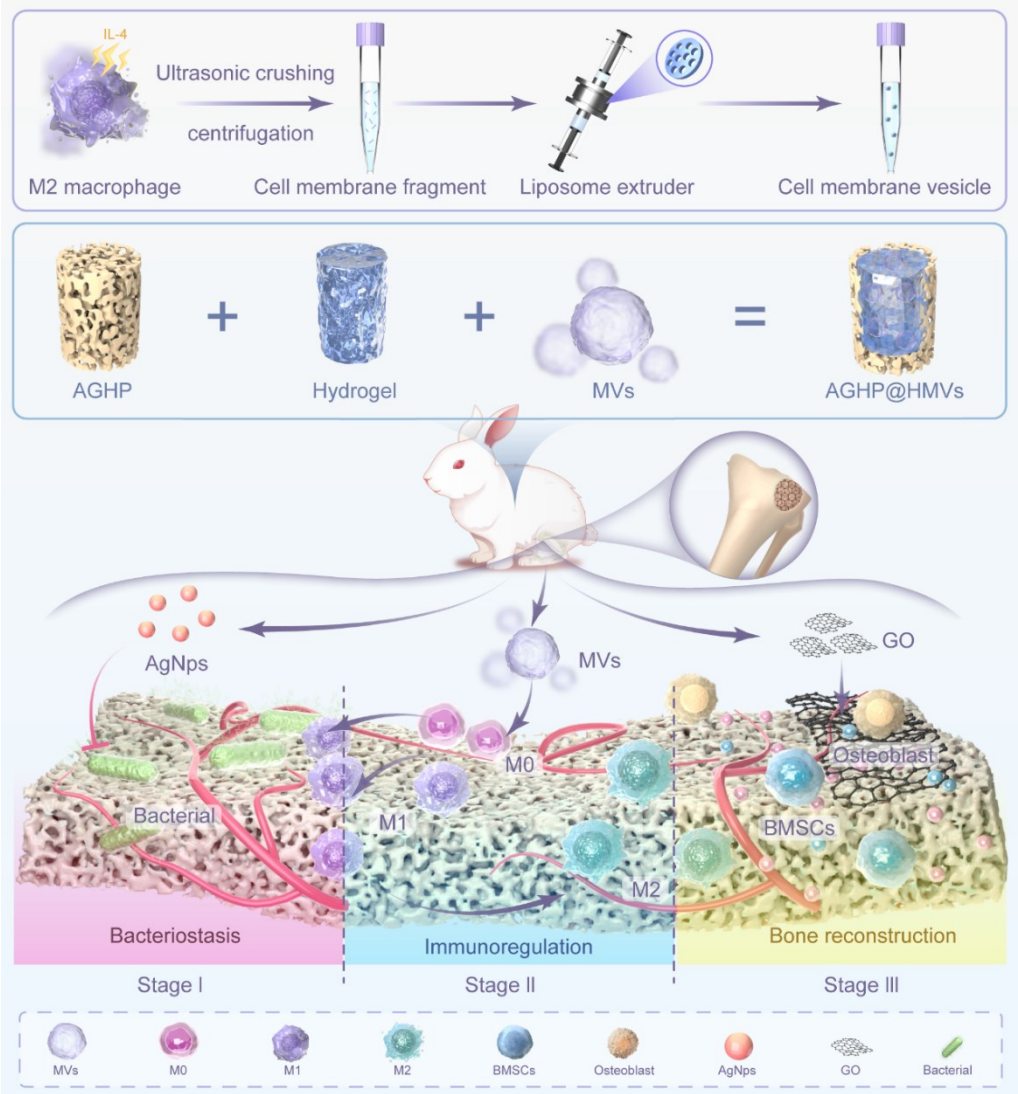

Scheme 1. Schematic diagram of the multi-effect integrated scaffold for infected bone defect repair. The AGHP@AMVs scaffold consists of AgNPs, GO nanosheets, sodium alginate hydrogel, MVs nanovesicles, and nHA/PEGDA matrix.

2. Results

2.1 Optimization of the concentration ratio of AgNPs with GO

To determine the appropriate concentration ratio of AgNPs in combination with GO, the AgNPs solution was treated with a 10-fold gradient concentration of MSCs for 1, 4, and 7 d, and then the Cell Counting Kit8 (CCK8) assay was performed. The results showed that when the concentration of AgNPs was over 10 μg/mL, it inhibited cell growth. As the concentration of AgNPs increased, it exhibited toxicity to cell growth (Figure S1A–B). Similarly, the cells were treated with GO solution. When the concentration of GO exceeded 1 μg/mL, the same phenomenon of inhibition of cell growth was observed, and this phenomenon was also concentration-dependent (Figure S1C). Subsequently, MSCs were treated with AgNPs at concentration gradients of 1, 5, and 10 μg/mL, and GO at concentration gradients of 0.1, 0.5, and 1 μg/mL for 1, 4, and 7 d to determine the CCK8, which was not significantly inhibited by AgNPs and GO at the highest ratio (10:1) (Figure S1D). The absorbance was measured at 600 nm at 6 h intervals for a total of 36 h. AgNPs mixed with GO at a ratio of 10:1 inhibited the growth of *Staphylococcus aureus* (*S. aureus*) (Figure S2A–C). A 10:1 ratio of AgNPs to GO was selected for the subsequent fabrication of the composite scaffolds.

2.2 Optimization of AGHP scaffold ratio and characterization of AGHP@AMVs scaffold

Scaffolds of 0.2AGHP, 0.5AGHP, and 1AGHP were used to treat *S. aureus* during the logarithmic growth period, and the absorbance at 600 nm was measured every 6 h for a total of 36 h. As the content of AgNPs and GO was increased, inhibition of bacterial growth began to occur in the 0.5AGHP scaffold group, and the inhibition was more pronounced when the content was higher (Figure S2D). The expression levels of the osteogenic genes alkaline phosphatase (*ALP*), Runt-related transcription factor 2 (*RUNX2)*, collagen I (*COLI*), and osteopontin (*OPN*) were detected using qPCR in the MSCs treated with the three scaffold groups via indirect co-culture. The results showed that the expression levels of osteogenic genes in the 0.2AGHP and 0.5AGHP groups were higher than those in the control group, while there was no significant difference between the 1AGHP group and the control group; the expression levels of osteogenic genes showed a decreasing trend with an increase in the content of AgNPs and GO (Figure S3A–D). Through screening, 0.5AGHP scaffolds were ultimately selected as the experimental subjects.

Porous AGHP scaffolds with triple periodic minimal surface structures were successfully fabricated using digital light printing. Field-emission scanning electron microscope (SEM) images further revealed the surface structure of the AGHP. A slightly rough and grainy scaffold surface was

observed with increasing magnification (**Figure 1**A). Elemental mapping analysis revealed the distributions of C, O, Ca, P, and Ag. The percentage of silver (Ag) content aligned with the initial amount added during fabrication, thereby confirming the presence of AgNPs in the scaffolds and their uniform distribution (Figure 1B). To observe the surface morphology of the sodium alginate hydrogels and the interfacial reaction between the scaffolds, and the scaffolds after filling the interior of the scaffolds, they were lyophilized and subjected to SEM scanning. The sodium alginate hydrogel exhibited a relatively uniform and highly interconnected network. A biphasic structure composed of a hydrogel, and a scaffold was observed when it was filled inside the scaffold (Figure 1C). Field-emission transmission electron microscopy (TEM) scanning after the fabrication of MVs using a liposome extruder revealed scattered hollow vesicle-like structures, and high expression of the macrophage M2 phenotype surface markers *CD163* and *CD206* was further detected using flow cytometry, confirming that the MVs were successfully prepared and originated from M2-type macrophages (Figure 1D). To confirm the successful piggybacking of MVs in sodium alginate hydrogels, the encapsulation rate of MVs in hydrogels was initially determined using the bicinchoninic acid assay (BCA) method, which showed that the encapsulation rate of MVs could reach 68.17% ± 2.82%. Subsequently, the composite hydrogel was prepared after the treatment of AMVs with 3,3'-dioctadecyloxacarbocyanine perchlorate and observed by 3D imaging under a laser confocal microscope, which showed that MVs were scattered in the hydrogel (Figure 1E). According to particle size analysis, the average size of the MVs was approximately 241.43 ± 10.45 nm, and only a single peak representing homogeneity was observed (Figure 1F).

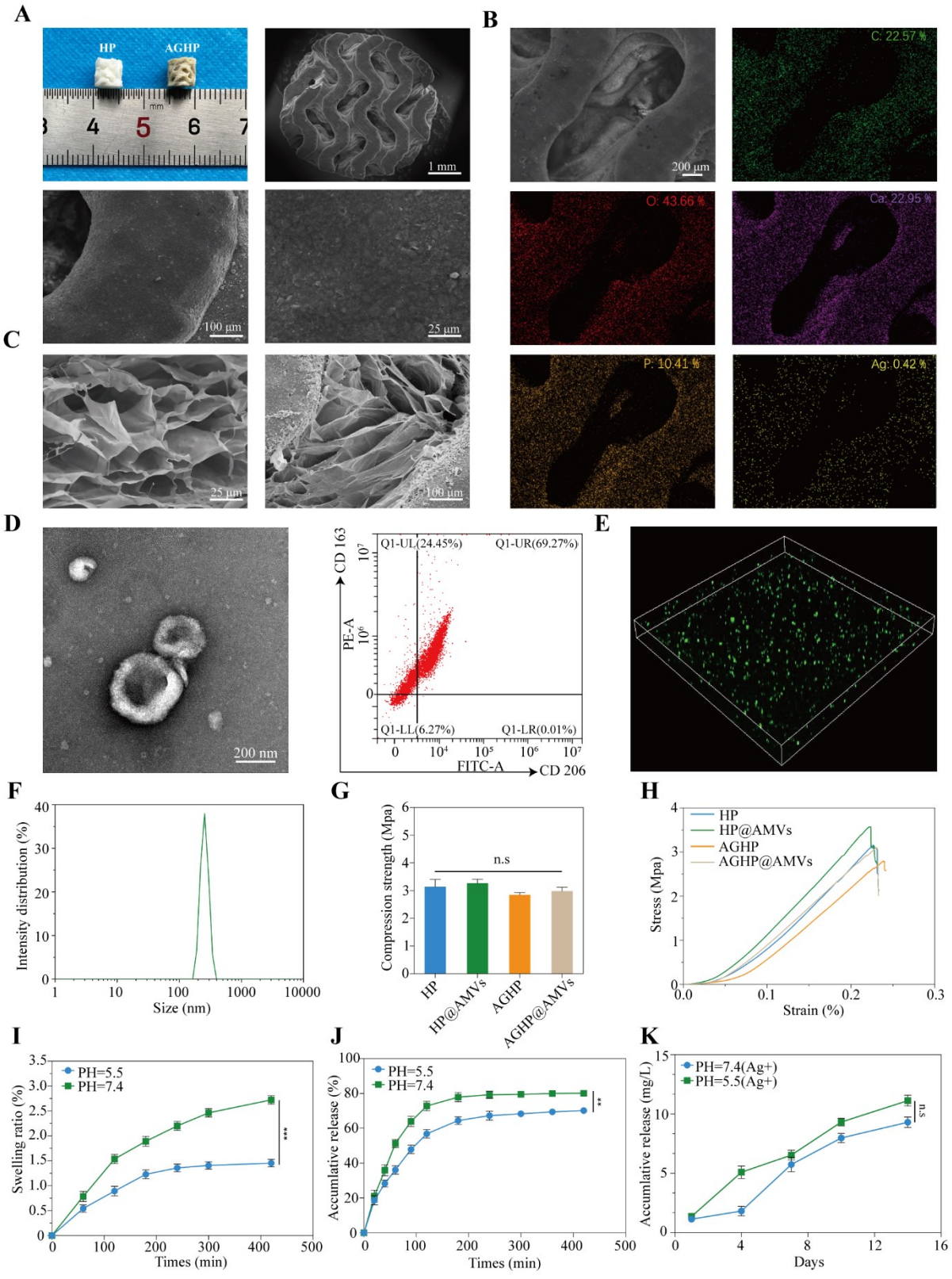

Figure 1. Physical characterization of AGHP@AMVs composite scaffolds. (A) Digital photographs of AGHP scaffolds and SEM images of different regions. (B) Elemental mapping images and EDS profiles confirming C, O, P, Ca, and Ag elements in the scaffolds. (C) SEM images of the hydrogel alone and AGHP@AMVs scaffolds. (D) TEM images of the MVs and the expression of *CD163* and *CD206* (M2 type macrophage marker) on the surface of MVs determined by flow cytometry. (E) Laser confocal detection of the loading of 3,3′-dioctadecyloxacarbocyanine-labeled MVs in hydrogels. (F) Particle size distribution of MVs. (G) Compressive strength of various composite scaffold scaffolds. (H) Compressive stress-strain curves of various composite scaffold scaffolds. (I) Solubility properties of sodium alginate hydrogel under different pH conditions. (J) Simulation of MVs release profile in AMVs by BCA method. (K) ICP detection of Ag^+ release from AGHP@AMVs under different pH conditions. n.s, no significance, *** P < 0.01, *** P < 0.001.*

The compressive properties of the scaffolds in each group were evaluated using a universal testing machine. The compressive strengths of HP, HP@AMVs, AGHP, and AGHP@AMVs were 2.87 ± 0.28, 3.21 ± 0.47, 2.65 ± 0.25, and 3.14 ± 0.15 Mpa, respectively, which were within the range of the compressive strength of normal cancellous bone. There was no statistical difference in compression strength between the groups. However, with the addition of AgNPs and GO, the compression strength showed a decreasing trend, and the filling of the hydrogel instead led to an increase in the compression strength; the changes in the stress-strain curves were in agreement with the results of compression strength (Figure 1G–H).

The infection results in a mildly acidic microenvironment. The effects of pH on the swelling properties of the hydrogels, drug release, and ion release from the scaffolds were further tested. The swelling of the hydrogels in an acidic environment (pH 5.5) was less than that in a neutral environment (pH 7.4) (Figure 1I), and the cumulative rate of the drug in an acidic environment was similar to that in a neutral environment (Figure 1J). This avoids the premature release of MVs from the hydrogel during the antimicrobial phase. The cumulative release of silver ions from the composite scaffolds was higher in the acidic environment than in the neutral environment (Figure 1K); however, there was no statistically significant difference between the two groups. This indicates that even with the filling of the hydrogel, there was no significant negative effect on the cumulative release of ions, which guarantees that the antimicrobial effect will not be significantly affected.

2.3 *In vitro* biocompatibility of composite scaffold

The effects of the composite scaffolds on the toxicity and proliferation of MSCs were evaluated using biocompatibility experiments. First, the groups of scaffolds were indirectly co-cultured with MSCs for 1, 4, and 7 d, and then CCK8 analysis was conducted. There was no significant difference in cell proliferation between groups (**Figure 2**D). Subsequently, the MSCs were treated in the same manner for 3 and 7 d before live/dead staining and counting. The staining and counting results showed that the cells grew well at the same time points in both groups, without a large number of dead cells (Figure 2A–B). Hemolysis assays were used to determine the suitability of the scaffolds, and the results showed no statistically significant differences in the rate of hemolysis between the different scaffolds and the negative control group (Figure 2C). All hemolysis rates were less than 1%, and no significant hemolysis was observed. To further investigate the extension behavior of the composite scaffolds on the cells, the scaffolds from each group were indirectly co-cultured with MSCs for 3 and 7 d, and cytoskeleton staining was performed. Over time, the cells in each group exhibited favorably elongated morphology, indicative of robust growth and proliferation (Figure 2E). The above experiments showed that all scaffold groups had appropriate biocompatibility, which is necessary for cell survival and tissue repair.

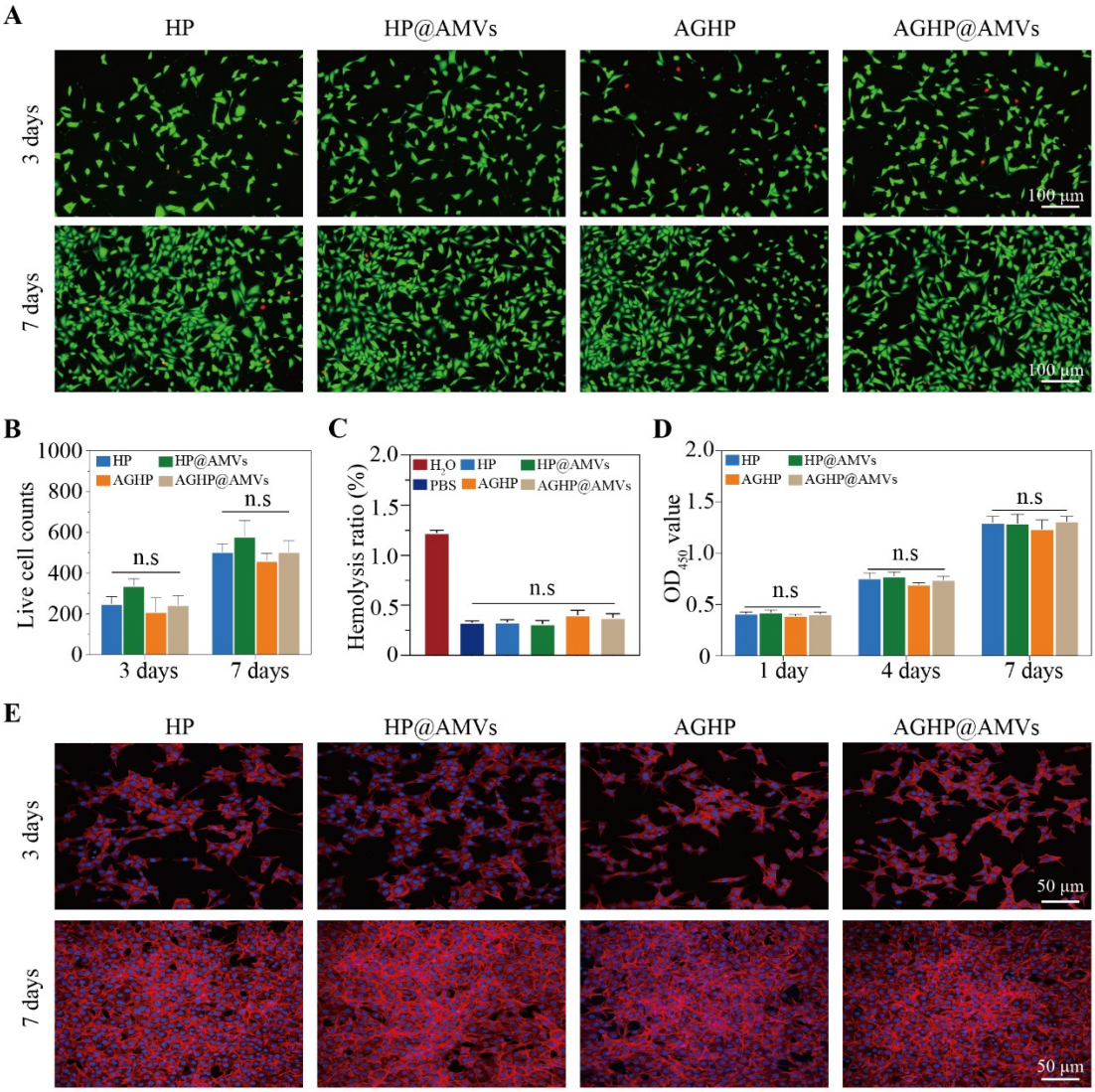

Figure 2. Biocompatibility of AGHP@AMVs composite scaffolds. (A) Live/dead results of MSCs treated with different scaffolds for 3 and 7 d. Green represents the living cells, and red on behalf of the dead cells. (B) Live cell counts were obtained from live/dead staining assays. (C) Hemolysis rate of different scaffolds. (D) CCK8 results of MSCs treated with different scaffolds for 1d, 4d, and 7d. (E) Cytoskeleton staining results. n.s, no significance.

2.4 *In vitro* antimicrobial activity and mechanism of composite scaffolds

To study the effects of the composite scaffolds on bacterial growth and broad-spectrum resistance, *S. aureus* and *Escherichia coli* (*E. coli*) were selected as gram-positive (G+) and gram-negative (G-) bacteria, respectively. First, the effect of each scaffold group on the bacterial growth was examined using a plate-counting method. The results showed that, owing to the presence of AgNPs, a more pronounced antimicrobial effect was present in the AGHP and AGHP@AMVs groups than in the HP and HP@AMVs groups. In addition, both scaffold groups filled with AMVs presented slightly more live bacterial colonies on Luria-Bertani (LB) agar plates than the scaffold-alone group (**Figure 3**A-C). Subsequently, the antimicrobial properties of the scaffold groups were examined using live/dead staining of the bacteria. The results were consistent with the plate counting experiments in that both composite scaffold groups containing AgNPs showed a large number of dead bacteria, and the AGHP@AMVs group exhibited a slightly lower bacterial mortality rate than the AGHP group (Figure 3J). The effect of the scaffolds on the bacterial growth in each group was further investigated using a bacterial growth inhibition assay. The results indicated that compared with the HP and HP@AMVs groups, the AGHP and AGHP@AMVs groups showed good inhibition of *S. aureus* and *E. coli* (Figure 3D–E). These results indicated that the AGHP@AMVs composite scaffolds exhibited a significant inhibitory effect on the growth of both G+ and G- bacteria, showing broad-spectrum antibacterial properties.

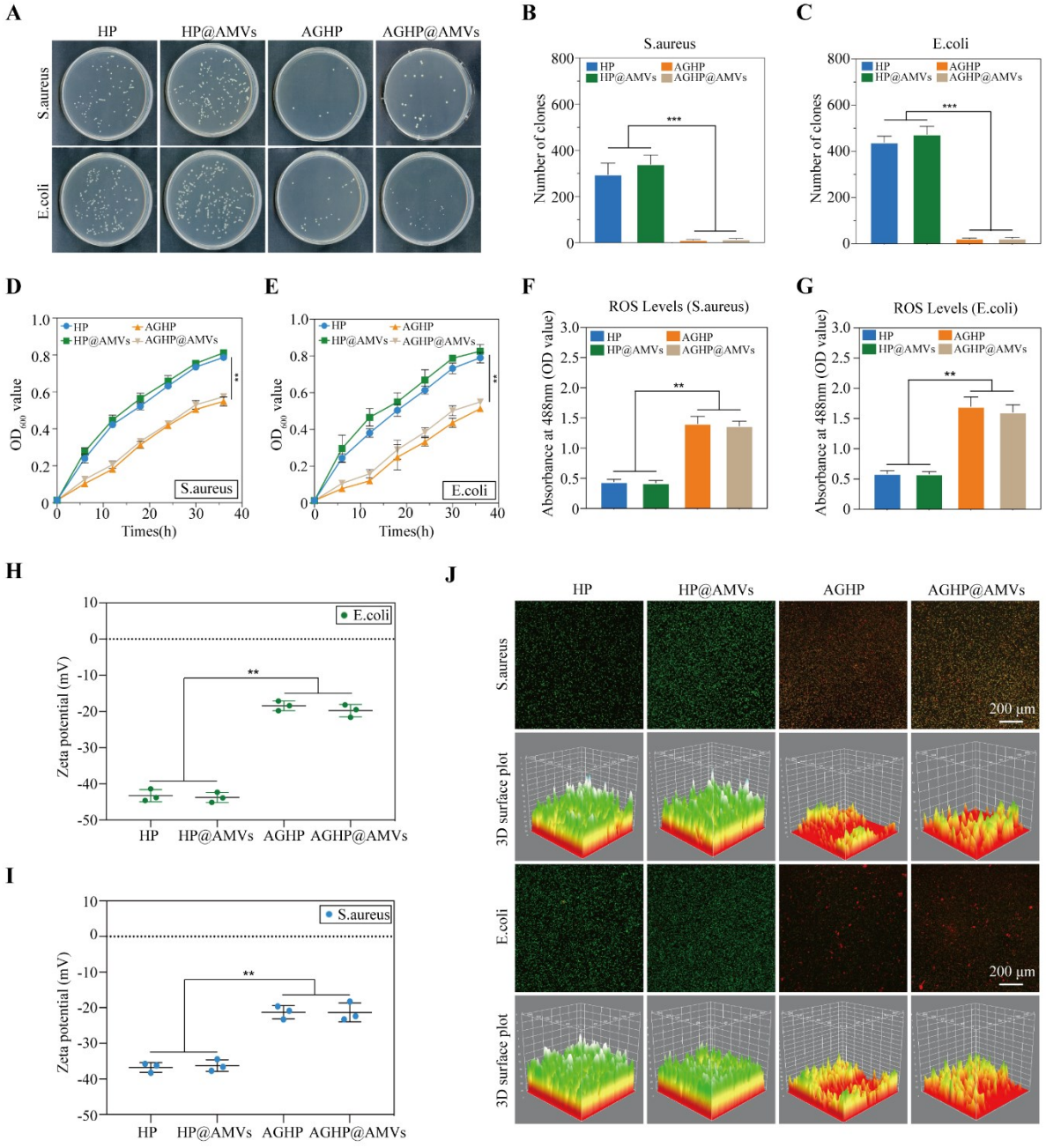

Figure 3. Antibacterial properties of AGHP@AMVs against *S. aureus* and *E. coli in vitro*. (A) Representative pictures of live colonies on standard agar plates after various composite scaffolds treated *S. aureus* and *E. coli*. (B-C) The colony counts were obtained from the agar plate. (D-E) Bacterial growth inhibition curves after different scaffolds treated *S. aureus* and *E. coli*. (F-G) ROS levels in *S. aureus* and *E. coli* treated with different scaffolds. (H-I) Zeta potential values of *S. aureus* and *E. coli* treated with different scaffolds. (J) Representative pictures of live/dead staining and 3D surface plot after different scaffold treatments of *S. aureus* and *E. coli*. *** P < 0.01, *** P < 0.001.*

The antibacterial mechanism of the composite scaffold was investigated by examining alterations in the concentration of ROS within bacterial cells and changes in the zeta potential of the bacterial surface. Analysis of ROS levels indicated significantly elevated expression in both *S. aureus* and *E. coli* when exposed to AGHP and AGHP@AMVs groups compared with the HP and HP@AMVs groups (Figure 3F–G). Moreover, zeta potential measurements demonstrated higher values for the AGHP and AGHP@AMVs groups *in S. aureus* (−21.27 ± 1.53 mV and −21.33 ± 2.18 mV, respectively) relative to the HP group (−36.77 ± 1.10 mV) and the HP@AMVs group (−36.27 ± 1.33 mV) (Figure 3H). Similarly, in *E. coli*, the zeta potentials of the AGHP and AGHP@AMVs groups (−18.43 ± 1.10 mV and −19.77 ± 1.40 mV, respectively) were markedly higher than those of the HP group (−43.26 ± 1.36 mV) and HP@AMVs group (−43.76 ± 1.15 mV) (Figure 3I). These findings indicate that the composite scaffold effectively eradicates bacteria by inducing ROS accumulation within the bacterial cells and modulating the bacterial surface membrane potential.

2.5 Immunomodulation of composite scaffold *in vitro*

Macrophages release anti-inflammatory and pro-repair cytokines by polarizing to the M2 phenotype, thereby creating a suitable microenvironment for tissue repair. To study the effect of composite scaffolds on the polarization state of macrophages, first, each group of scaffolds was co-cultured with RAW264.7, and the polarization state of macrophages as well as the recruitment effect on MSCs was detected using a cell migration assay. The results showed that both the AGHP@AMVs and HP@AMVs groups exhibited significant chemotaxis toward MSCs (**Figure 4**A). Quantitative results of the migrating cells confirmed this result (Figure 4B). The release of MVs from the composite scaffolds promoted macrophage polarization toward the M2 phenotype. Subsequently, two surface markers of M2-type macrophages, *CD206* and *CD163*, were detected using flow cytometry to further investigate the effect of the composite scaffolds on macrophage polarization. After 3 d of treatment, the proportions of M2-type macrophages in the AGHP@AMVs and HP@AMVs groups were 12.58% and 7.51%, respectively, whereas the proportions in the AGHP and HP groups were only 3.64% and 2.04%, respectively. After 7 d, the proportions of M2 macrophages in the AGHP@AMVs and HP@AMVs groups reached 66.29% and 53.39%, respectively, whereas those in the AGHP and HP groups were only 23.18% and 8.45%, respectively (Figure 4C).

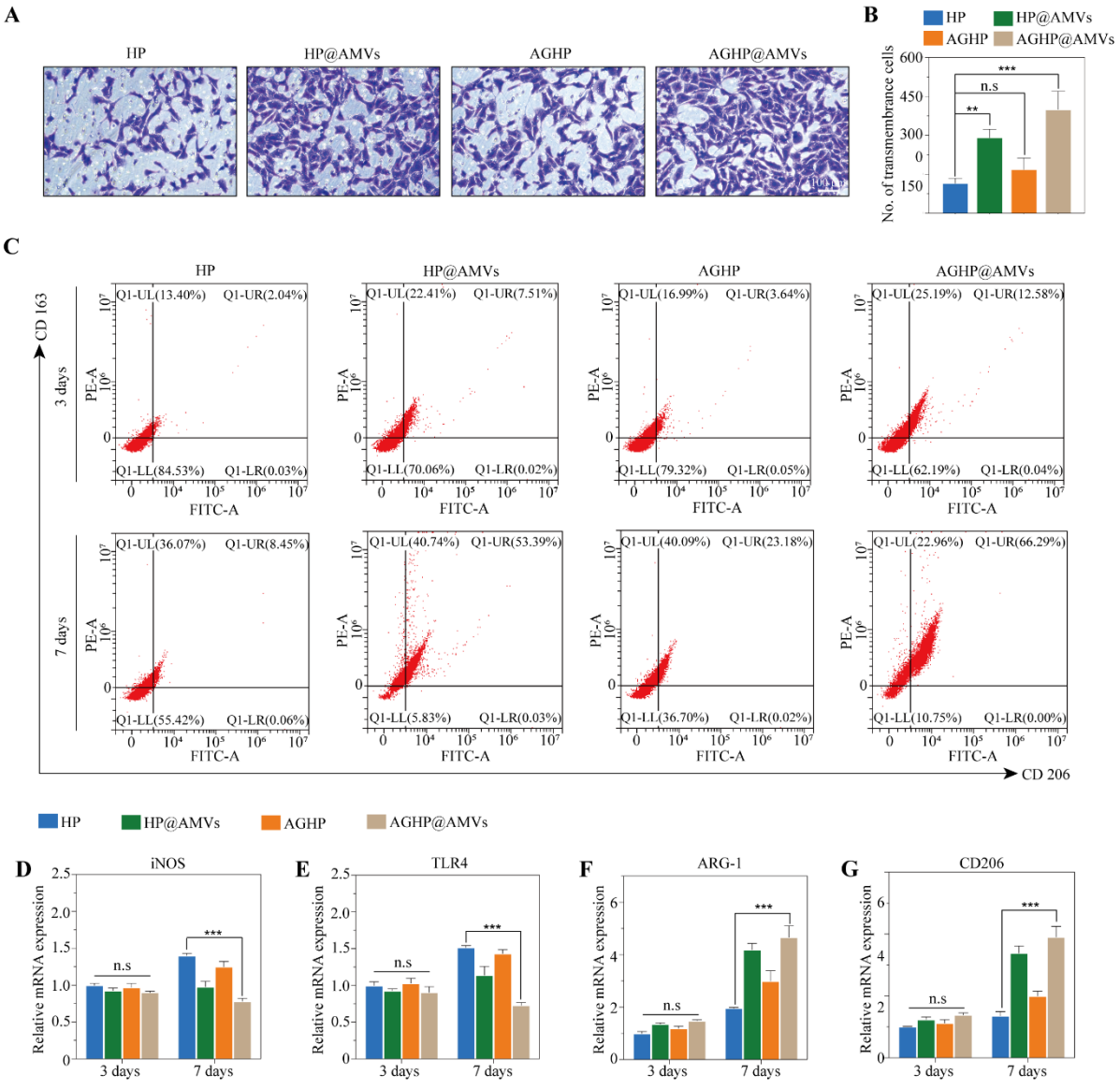

Figure 4. Immunomodulatory effects of AGHP@AMVs composite scaffolds *in vitro*. (A) Transwell assay to analyze the migratory behavior of various scaffolds co-cultured with RAW264.7 cells on MSC cells. (B) Migrating cell counts obtained from the transwell assay. (C) Flow cytometry to determine the expression of *CD163* and *CD206* (M2 phenotypic macrophage markers) in various scaffolds treated with RAW264.7 cells for 3 and 7 d. (D-E) Relative mRNA expression of M1-type macrophage-associated genes in various scaffold-treated RAW264.7 cells for 3 and 7 d. (F-G) Relative mRNA expression of M2 phenotypic macrophage-associated genes in various scaffold-treated RAW264.7 cells for 3 and 7 d. n.s, no significance, *** P < 0.01, *** P < 0.001.*

The expression of genes associated with M1-type and M2-type macrophages was analyzed using quantitative qRT-PCR after 3 and 7 d. No significant differences in the expression levels of both M1-type and M2-type macrophage-associated genes were observed between the groups on day 3. After treatment for 7 d, the *CD 206* and *ARG1* representing the M2 phenotype were more highly expressed in the AGHP@AMVs group than in the HP group, indicating a higher proportion of M2 macrophages. In contrast, the expression of the M1-type macrophage-associated genes inducible *iNOS* and *TLR4* was suppressed in the AGHP@AMVs group (Figure 4D–G). These results provide reliable evidence that the prepared AGHP@AMVs scaffolds possess immunomodulatory properties.

2.6 *In vitro* osteoinductive activity of composite scaffold

Osteogenic differentiation is an important process that affects bone regeneration. The effect of the composite scaffolds on osteogenic differentiation was assessed using alkaline phosphatase (ALP) and alizarin red S (ARS) staining. All samples cultured in osteoinductive medium showed positive ALP staining at the indicated time points. The AGHP@AMVs scaffolds exhibited the highest osteogenic capacity after 7 and 14 d of culture, whereas the HP and AGHP scaffolds had similar osteogenic effects. The quantitative ALP activity values were consistent with the staining results (**Figure 5**A–B). ARS staining was used to analyze the mineralization stage of osteogenic MSCs in the different groups by staining the calcium nodules. According to ARS staining, based on gross and microscopic observations, the red color deepened in each group with incubation time and presented the highest level of mineralization with a dense distribution of calcium nodules in the AGHP@AMVs group. Similarly, the quantitative ARS staining values were consistent with the staining results (Figure 5C–D).

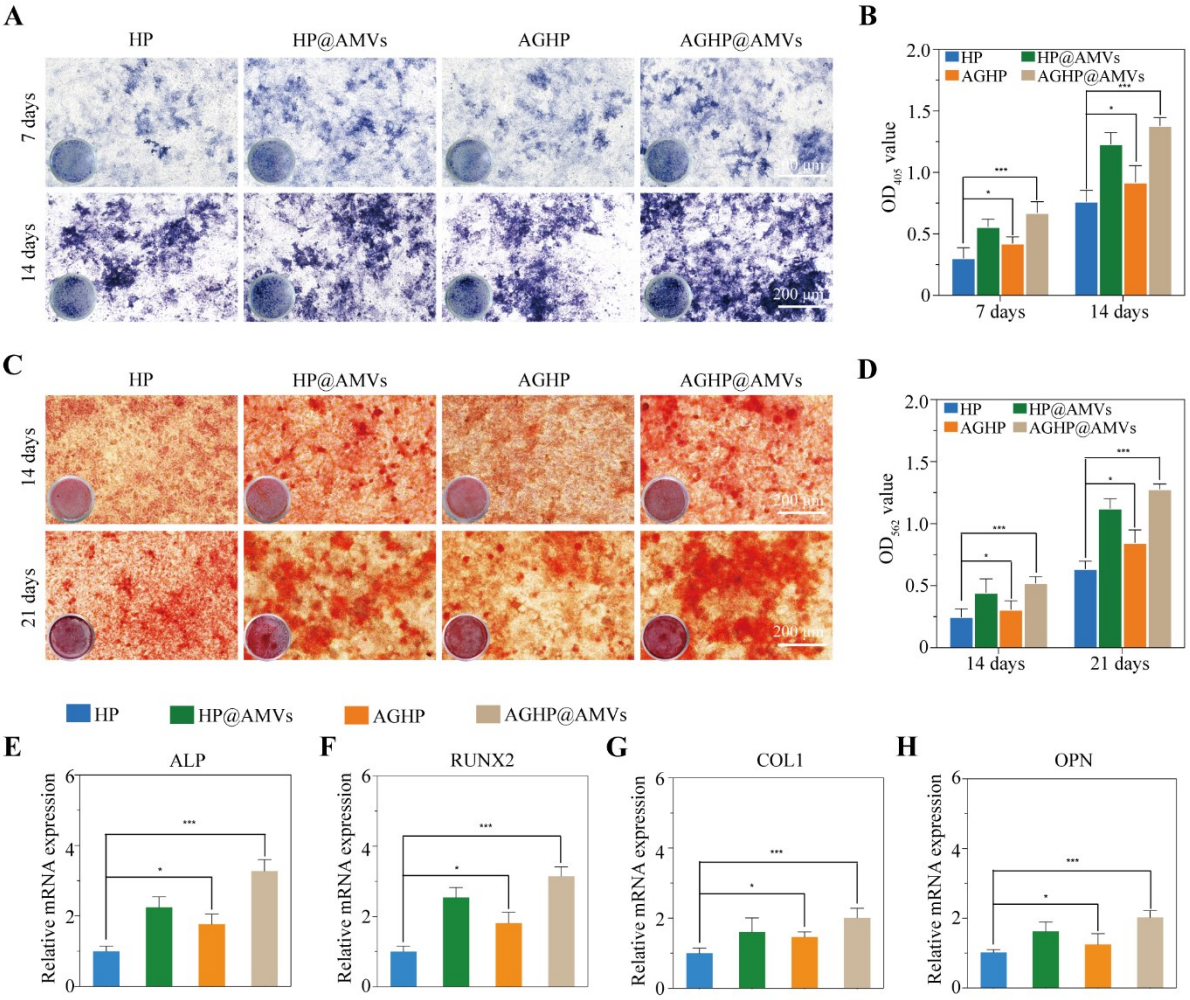

Figure 5. Osteogenic activity of MSCs co-cultured with various scaffolds *in vitro*. (A) Microscopic and gross images of ALP staining of MSCs co-cultured with various scaffolds after 7 and 14 d. (B) Quantitative results were obtained from ALP staining on 7 and 14 d. (C) Microscopic and gross images of ARS staining of MSCs co-cultured with various scaffolds on 7 and 14 d. (D) Quantitative results were obtained from ARS staining on 14 and 21 d. (E-H) qRT-PCR assay for the expression of osteogenesis-related genes in MSCs after 14 d of co-culture of MSCs with various scaffolds, including *ALP* (E), *RUNX2* (F), *Col I* (G), and *OPN* (H). *$p < 0.05$, *** $p < 0.001$.*

In addition, the osteoinductive activity of the composite scaffolds was further investigated using qRT-PCR to determine the expression of relevant osteogenic genes in different scaffold groups, including *ALP*, *RUNX2*, *COLI*, and *OPN*. The results showed that compared with the HP group

scaffolds, the scaffolds in the HP@AMVs, AGHP, and AGHP@AMVs groups significantly upregulated the expression of *ALP*, *RUNX2*, *COLI*, and *OPN* genes but at different levels, which sufficiently proved that the composite scaffolds could enhance osteogenic differentiation (Figure 5E–H). The above experiments showed that the composite scaffolds exhibited effective osteoinductive activity.

2.7 *In vivo* assessment of composite scaffold for bone regeneration

The promising *in vitro* antimicrobial, immunomodulatory, and osteogenic properties of the AGHP@AMVs scaffold prompted us to explore their potential roles and mechanisms (**Figure 6**A). First, an infected bone defect model was established in the proximal tibia of the rabbits (Figure 6B), and abscess formation was observed in the proximal tibia after 14 d (Figure S4A). The peripheral proliferative and bone tissues of the model were subjected to HE staining, and the bone marrow cavity was flushed for bacterial culture. The results showed that a large number of inflammatory cells infiltrated the peripheral proliferative tissues (Figure S4C), and bone tissue sections showed bone loss and trabecular bone disruption (Figure S4B). LB agar culture plates also showed high bacterial growth (Figure S4D). To further evaluate new bone formation *in vivo* after implantation of the composite scaffold, micro-CT sweeps of the proximal right tibia of rabbits were performed, and three-dimensional reconstruction was performed at four and eight weeks. After four weeks, only a small amount of new bone was formed at the defect site in the Blank, HP, HP@AMVs, and AGHP groups. In contrast, the AGHP@AMVs group exhibited milder symptoms of infection and increased new bone formation. At eight weeks, the AGHP group showed a reduction in infection symptoms, but there was still a more pronounced unrepaired gap at the defect site. Infection was not significantly improved in the Blank, HP, and HP@AMVs groups, and there was less new bone formation at the defect site than in the AGHP group. In contrast, infection symptoms were significantly reduced, and significant new bone formation was observed around the defects in the AGHP@AMVs group (Figure 6C). Quantitative analysis confirmed that the AGHP@AMVs group exhibited higher bone density (BMD), bone volume/total volume (BV/TV) and trabecular bone number (Tb. N), and lower trabecular separation (Tb. Sp) values compared with the other groups (Figure 6D–G). The AGHP@AMVs composite exhibits robust osteogenic capacity.

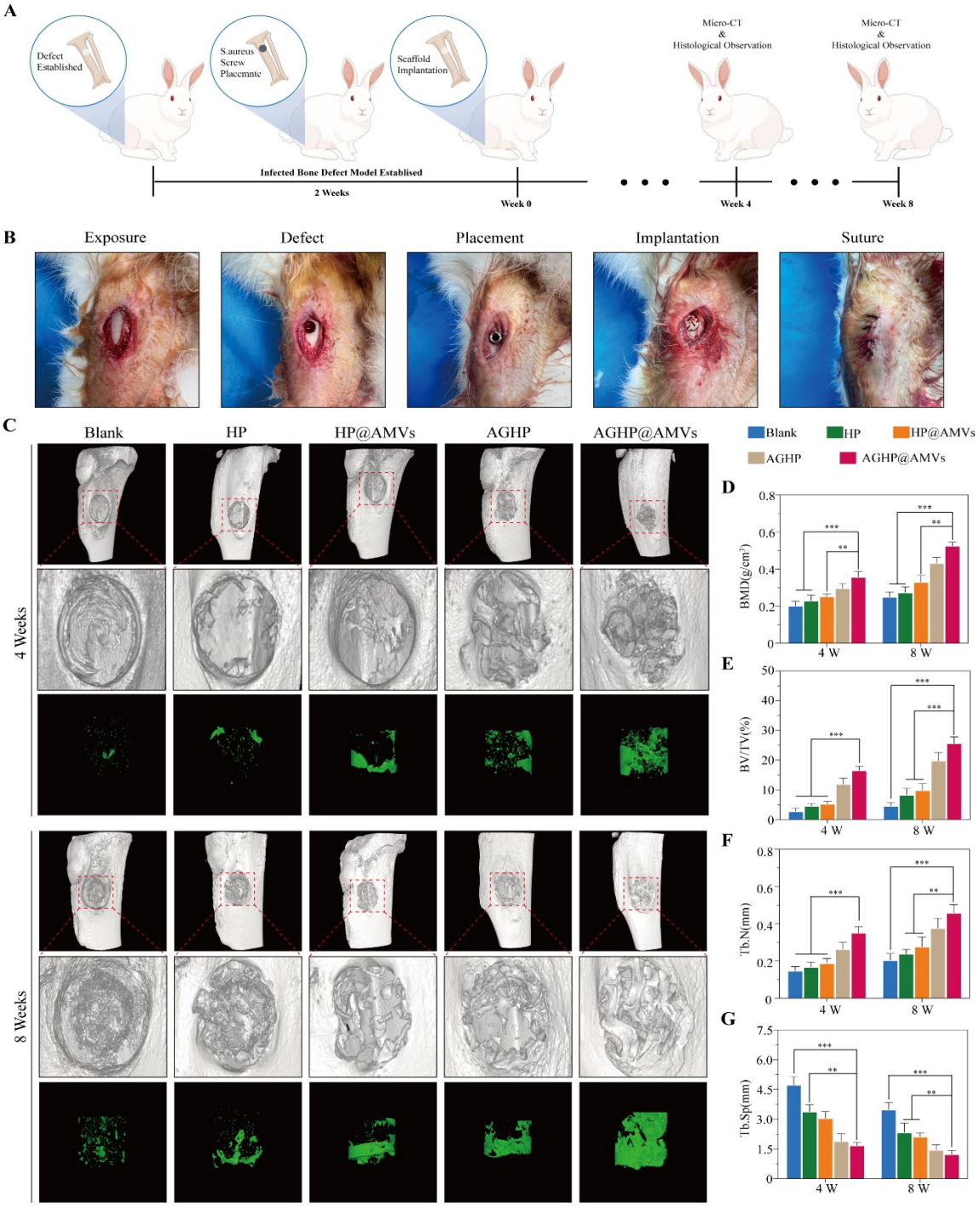

Figure 6. Systematic evaluation of the osteogenic effect of AGHP@AMVs scaffolds *in vivo*. (A) Schematic representation of the construction and treatment of infected proximal tibial defects in New Zealand rabbits. (B) Schematic diagram of the experimental procedure. (C) Reconstructed micro-CT images of New Zealand rabbit tibia after 4 and 8 weeks of treatment with various stents. (D-G) Quantitative analysis of BMD (D), BV/TV (E), Tb. N (F), and Tb. Sp (G). All statistics are

expressed as mean ± SD (n = 3, ***P < 0.01 and ***P < 0.001*).

2.8 *In vivo* assessment of composite scaffold for antimicrobial, immunomodulatory, and osteogenesis activities

HE and Masson staining were used to evaluate the effect of the AGHP@AMVs composite on bone histology and regeneration in the area of the infected bone defects in the proximal tibia. The results showed that after four weeks, the Blank, HP, and HP@AMVs groups appeared to limit the generation of new bone, whereas the AGHP@AMVs group exhibited more new bone and fibrous tissue around the defect. Eight weeks after scaffold implantation, considerable new bone tissue was observed in the AGHP@AMVs group, growing from the edge of the defect area toward the central area and partially bridging with the implant, suggesting that the porous structure of the scaffold was critical for osteogenesis (**Figure 7**A). Eight weeks after implantation, there was no obvious interface between the implant and host bone, further indicating that the AGHP@AMVs composites promoted bone mineralization and osseointegration. Masson staining results also indicated that the AGHP@AMVs composites were effective in promoting the production of collagen and mineralized bone (Figure S5). To observe the *in vivo* antimicrobial effects of the AGHP@AMVs composites, the bone tissues around the implants were collected and subjected to Gram staining. The results showed that Gram staining of the Blank, HP, and HP@AMVs groups revealed more bacteria, whereas the AGHP and AGHP@AMVs groups had much fewer bacteria at eight weeks after surgery (Figure 7B). Composite scaffolds containing AgNPs exhibit effective antibacterial properties. Finally, the immunomodulatory effects of the composite scaffolds *in vivo* were investigated using immunohistochemistry for *iNOS* and *CD206*. Consistent with the *in vitro* qRT-PCR results, the expression level of *iNOS* significantly decreased and that of *CD206* significantly increased in the bone defect region after treatment with AGHP@AMVs scaffold at eight weeks after surgery (Figure 7D–F). The AGHP@AMVs scaffold effectively suppressed inflammation by transforming macrophages from the pro-inflammatory (M1 phenotype) to the anti-inflammatory (M2 phenotype) stage, thereby providing a favorable effect for the favorable environment for subsequent bone defect repair. Further histological HE staining was performed to analyze the internal organs (heart, liver, spleen, lungs, and kidneys) of the rabbits. None of the scaffolds in each group caused obvious pathological changes in the organs (Figure S6). This indicates that the prepared scaffolds are relatively safe in animals. The above results provide convincing evidence that the AGHP@AMVs composite scaffold

system has excellent antimicrobial properties and immunomodulatory effects and also possesses excellent osteoinductive, osteoconductive, and osseointegrative properties.

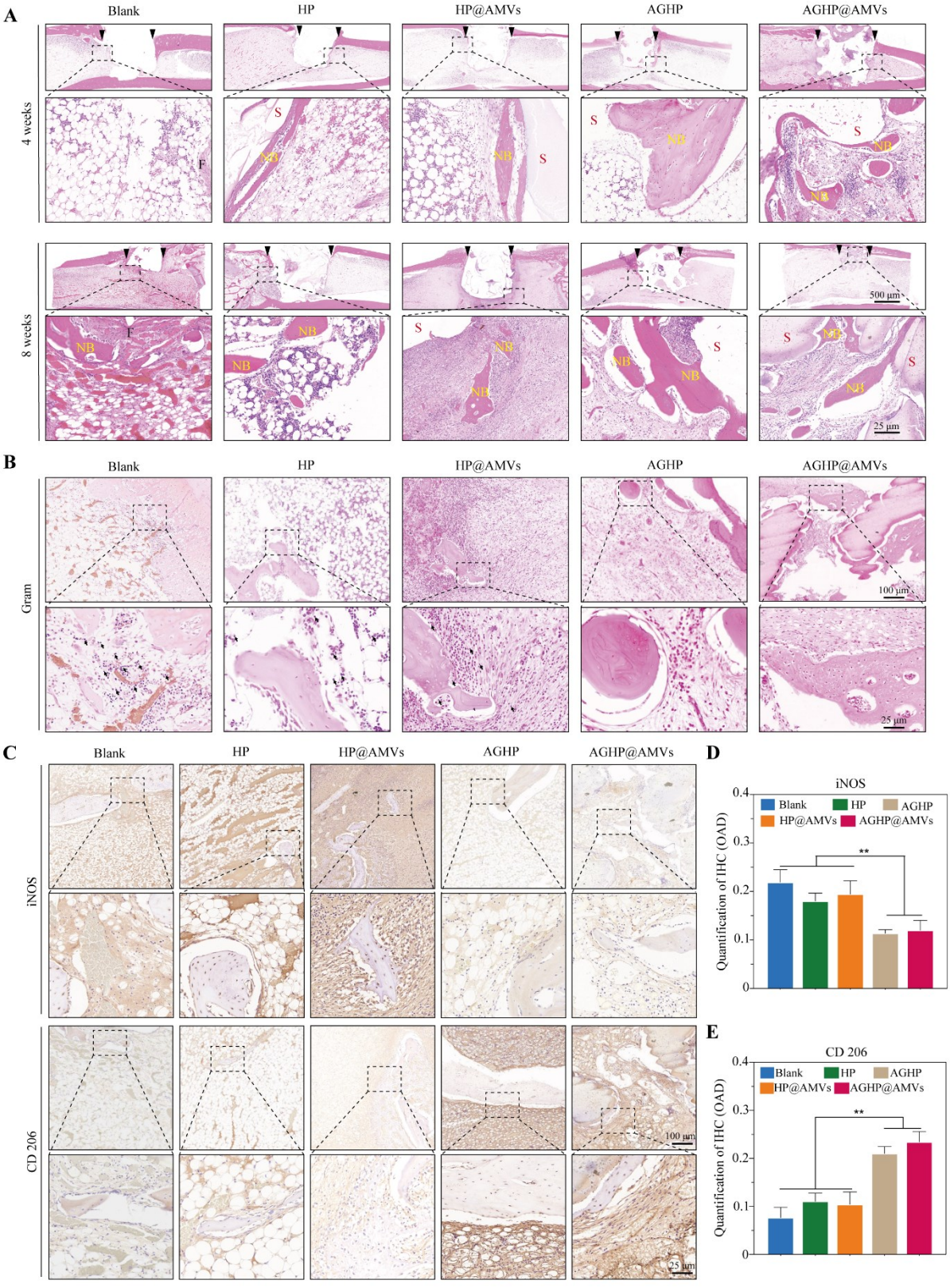

Figure 7. Histological and immunohistochemical assessment of antimicrobial, immunomodulatory and osteogenesis of AGHP@AMVs composite scaffolds *in vivo*. (A) HE staining images show the formation of new bone in the Blank group and the other four experimental groups at 4 and 8 weeks postoperatively. The black triangles define the boundaries of infected bone defects. (F, fibrous tissue; NB, newly formed bone tissue; S, scaffold residue).

2.9 RNA-seq analysis of the immunoregulatory mechanism of MVs and osteogenesis mechanism of GO

We further validated the immunomodulatory effects of AGHP@AMVs scaffolds and revealed the mechanism underlying the induction of bone tissue regeneration and related biological events. The HP and AGHP@AMVs scaffolds were used as the control and experimental groups, respectively. RAW264.7 and MSCs were treated for different times, and RNA sequencing was performed. RAW264.7 cells were treated with AGHP@AMVs scaffold for 3 d, and RNA-seq results showed that genes related to M1 and M2 polarization, such as *IL-1β*, *iNOS*, *ARG1*, and *TGF-β*, were not significantly changed (**Figure 8**A). KEGG pathway enrichment analysis did not show alterations in the pathways involved in macrophage polarization (Figure 8B). However, 7 d after treatment of RAW264.7 cells with AGHP@AMVs, RNA-seq results showed that the expression of M1 polarization-related genes (*CXCL10*, *IL-1β*, *iNOS*, *IFN-β*, and *TNF-α*) was downregulated, while the expression of M2 polarization-related genes (*ARG1*, *MRC1*, *YM1*, *TGF-β*, and *IL-1rα*) was upregulated (Figure 8C). Simultaneously, the KEGG pathway enrichment analysis indicated alterations in macrophage polarization-related pathways such as the TNF, JAK-STAT, mTOR, and NF-κ B signaling (Figure 8D). Western blotting and nucleoplasmic separation experiments were performed to verify the effects of the composite scaffold on the top 4 inflammation-related pathways and their key proteins. Western blot results showed that the overall expression levels of key proteins *STAT3*, *p-STAT3*, and mTOR in the JAK-STAT and mTOR signaling pathways were not significantly altered in the MVs group compared with the control group. However, in the TNF signaling pathway, the expression level of the key protein *TNFα* was lower in the MVs group than in the control group. Additionally, in the NF-κB signaling pathway, the expression level of the key protein *IκBα* was higher in the MVs group than in the control group (Figure 8E–F). The activation of the NF-κB signaling pathway occurs through the degradation of *IκBα*, leading to the entry of the P50/P65 complex into the nucleus. *RelA* expression levels in the cytoplasm and nucleus were analyzed using a nucleoplasmic separation assay. The

findings revealed that *RelA* was mainly localized in the cytoplasm of the MVs group, in contrast to the control group (Figure 8G–H). These results suggest that MVs in composite scaffolds can be immunomodulated by inhibiting the activation of the TNF and NF-κB signaling pathways.

In addition, RNA-seq results of MSCs treated with the AGHP@AMVs scaffold for 10 d showed that there were 3092 differentially expressed genes in the volcano diagram, of which 2624 were upregulated and 664 were downregulated (Figure 8I). The heat map showed that the expression of osteogenesis-related genes, such as *RUNX2* and *OCN*, was upregulated in the AGHP@AMVs scaffold group (Figure 8J). KEGG pathway enrichment analysis highlighted significant changes in the osteogenesis-related signaling pathways, with the most notable alteration observed in the Wnt signaling pathway (Figure 8K). Western blotting and TEC/LEF 1 detection were used to further explore the effect of each component in the composite scaffold on the Wnt/β-catenin signaling pathway. The results showed that the β-catenin expression level of MVs and GO group is much higher than the control group and AgNPs (Figure 8L–M). Simultaneously, the MVs and GO groups effectively promoted the activation of TCF/LEF 1 compared with the control and AgNPs groups (Figure 8N). These results suggest that GO can exert an osteogenic effect by activating the Wnt/β-catenin signaling pathway, and MVs can exert a synergistic effect with the osteoinductive activity of GO.

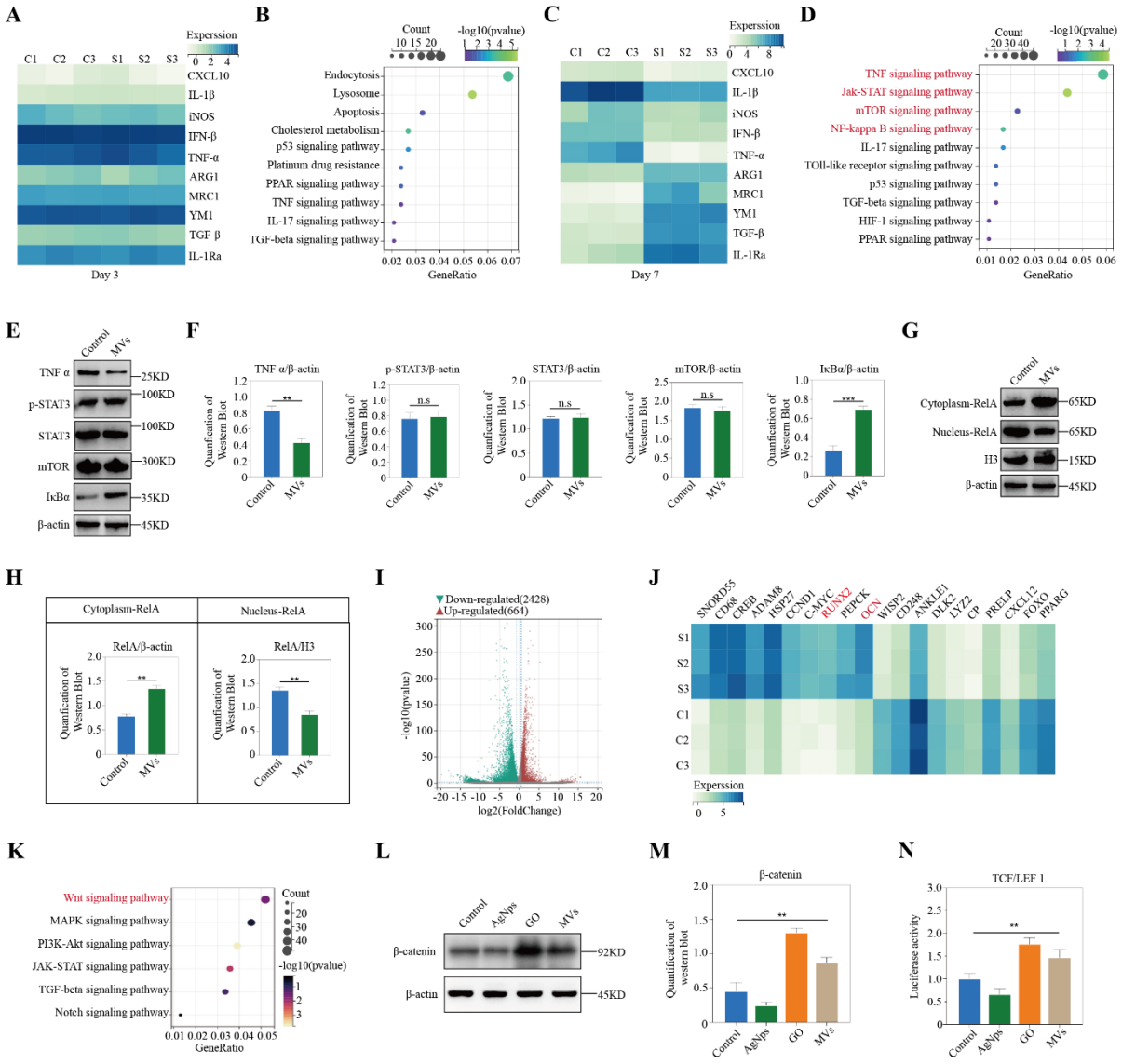

Figure 8. Analysis of scaffold-mediated gene expression and cell signaling pathways during macrophage polarization and osteogenic differentiation of MSCs. (A) Heatmap of macrophage polarization-related differential genes in AGHP@AMVs group compared to HP group after 3 d of scaffold treatment of RAW264.7 cells. (B) Bubble plot showing the changes of signaling pathways related to inflammation after 3 d of treatment of RAW264.7 cells with AGHP@AMVs group compared with HP group. (C) Heatmap of macrophage polarization-related differential genes in AGHP@AMVs group compared to HP group after 7 d of scaffold treatment of RAW264.7 cells. (D) Bubble plot showing the changes of signaling pathways related to inflammation after 7 d of treatment of RAW264.7 cells with AGHP@AMVs group compared with HP group. (E) Western blotting detects the protein expression levels of *TNFα*, *STAT3*, *p-STAT3*, *mTOR*, and *IκBα*. (F)

Quantification of western blotting. (G) Nucleoplasmic separation to detect the expression level of *RelA* in cytoplasm and nucleus. (H) Quantification of nucleoplasmic separation. (I) Volcano plot showing differentially regulated genes in the AGHP@AMVs group compared to the HP group. (J) Heatmap of differentially regulated genes related to osteogenesis in the AGHP@AMVs group compared to the HP group. (K) Bubble plot showing the changes in signaling pathways related to osteogenesis in the AGHP@AMVs group compared to the HP group. (L) Western blotting to detect the differences in the expression of total β-catenin in the Wnt/β-catenin pathway with each component in AGHP@AMVs. (M) Quantification of Western blotting. (N) Detection of the composite scaffold components with luciferase activity of TCF/LEF 1. n.s, no significance, ***P < 0.01, ***P < 0.001.*

3. Discussion

The repair of infected bone defects is a complex and orderly process that includes two major processes: infection control and bone reconstruction.[34] Immunomodulation runs through all stages of tissue repair, and bone repair is no exception. They can adjust the immune environment at different stages to achieve an immune balance by mediating the interaction between immune cells and bone cells.[22] Antibiotic-loaded biologically active scaffolds are commonly used to repair infected bone defects.[35] However, the side effects of antibiotics, bacterial resistance, and biomaterial selection for bone reconstruction are issues that need to be addressed. In recent years, the excellent antibacterial performance of AgNPs has effectively compensated for the shortcomings of antibiotics; however, their concentration-dependent characteristics limit their safe application in organisms.[8] nHA, which is similar to apatite in natural bone, can induce osteogenesis *in vitro* and *in vivo* and has been used safely for several years.[36] However, the compressive strength of a simple nHA scaffold is low, usually between 0.17–0.64 Mpa,[37] which makes it difficult to meet the mechanical properties required for bone reconstruction. GO provides a new strategy for the application of bone tissue engineering scaffolds due to its excellent physicochemical properties and osteoinductive activity.[38] Unfortunately, GO is also concentration-dependent, and its excessive addition can have negative effects on organisms. To address these issues, we constructed a multi-effect integrated composite scaffold by adding appropriate ratios of AgNPs and GO to HP scaffold and loading M2-type macrophage MVs.

Appropriate concentrations are a prerequisite for AgNPs and GO to exert ideal biological effects. *In vitro* cytotoxicity experiments detected that cell growth was inhibited when the concentration of AgNPs exceeded 10 μg/mL and GO surpassed 1 μg/mL. This is consistent with the findings of Dong et al.[39] and Li et al.[40] and is attributed to the fact that high concentrations of AgNPs tend to accumulate rapidly in cells, leading to rapid cell death by denaturing proteins.[41] In contrast, GO can lead to cell disintegration through the physical cutting of cells by the sharp surface and the extraction of the lipid bilayer of the cell membrane.[42]Subsequently, the appropriate ratio of AgNPs to GO was determined using bacterial growth inhibition experiments. Finally, the scaffolds were screened using cytotoxicity experiments and the expression levels of relevant osteogenic genes were to be used in subsequent experiments with AgNPs at 0.5 wt% and GO at 0.05 wt%.

Scaffolds for repairing infected bone defects in bone tissue engineering must not only exhibit effective antimicrobial properties and osteoinductive activity but also provide essential mechanical support. Owing to the favorable mechanical properties of GO, the compressive strength of the AGHP@AMVs composite scaffolds prepared in this study was effectively improved compared with that of the pure nHA scaffolds. The excellent killing performance of AGHP@AMVs against G+ and G- bacteria illustrates that the AgNPs in the scaffolds hydrolyze the silver ions at an effective concentration and interact with the bacterial surfaces, which disrupts the bacterial cell membrane's charge balance,[10, 11, 43] further disrupting the basic life activities of the bacteria and inducing the overproduction of ROS in the bacteria,[12, 13, 44] ultimately leading to their rupture and death. In addition, we observed greater bacterial survival with AGHP@AMVs than with AGHP. This may be due to the polysaccharide structure in the sodium alginate hydrogel that provides a physical barrier for the bacteria, and its good permeability also provides a favorable environment for the exchange of nutrients between the bacteria and the external environment.[45] Therefore, the use of sodium alginate hydrogel as a capture agent to recruit bacteria for further killing of bacteria and subsequent colonization of MSCs is a favorable solution. In animals, we found that AGHP@AMVs effectively promoted the expression of osteogenesis-related genes, ALP activity, and the formation of mineralized nodules. Micro-CT and sectional staining also revealed effective osteoinductive activity. This is because of the high specific surface area of GO, which effectively promotes cell adhesion[46]. In addition, the surface of GO contains a large number of hydrophilic groups such as carboxyl, hydroxyl, and epoxy groups.[47] These groups can induce the adsorption of protein molecules and osteogenesis-related factors onto the functional groups of protein molecules through electrostatic and van der Waals' forces,[48] which in turn affect the differentiation of osteoblasts. After eight

weeks of *in vivo* observation, no significant pathological changes were observed in the various organs of the animals. This delivery strategy provides data supporting the safe application of AgNPs and GO *in vivo*.

Immunocytokine delivery is one of the most commonly used immunomodulation methods. The complex physiological environment in the body affects cytokine activity and the retention cycle, thereby influencing the therapeutic effects. Artificially fabricated cell membrane nano-vesicles are more conducive to stable and efficient cellular uptake while eliminating the need to consider biocompatibility and immune rejection.[49] Relevant studies have indicated that the presence of infection induces a weakly acidic pH in the surrounding environment, approximately 5.5.[50] The pH responsiveness of sodium alginate was used to construct a delivery system for MVs. The solubility of sodium alginate hydrogel in an acidic environment was lower than that in a neutral environment, and the release of MVs from the hydrogel was delayed. This is consistent with a report by Liu et al.[51] which prevented the pro-inflammatory environment required for the antimicrobial phase from being compromised. In addition, AGHP@AMVs were effective in promoting MSCs migration, reducing the expression of pro-inflammatory genes, and remodeling macrophages to an M2 phenotype. This may be attributed to the proteins associated with the surface of MVs. When in contact with homologous macrophages, enhanced interactions with the cells repolarize the macrophages and then further polarize them toward the M2 phenotype.[52]

The most important aspect of the clinical translational application of bone tissue engineering scaffolds is the need to clarify the interactions between materials and cells. Although relevant studies have confirmed that GO can promote the differentiation of MSCs toward osteogenesis,[33, 53] the relevant molecular mechanism of its promotion of osteogenesis remains unclear. Next, we verified the effect of the AGHP@AMVs composite scaffolds on macrophage polarization using high-throughput sequencing and elucidated the potential mechanism of GO as a component in osteogenesis. We found that AGHP@AMVs acted on cells for 7 d before inducing changes in the macrophage polarization status and inflammation-related pathways. Western blotting and nucleoplasmic separation experiments further demonstrated that MVs suppress inflammatory responses by inhibiting the activation of TNF and NF-κB signaling pathways. In addition, we found that multiple osteogenesis-related pathways were altered after AGHP@AMVs treatment of MSCs, among which the Wnt/β-catenin signaling pathway ranked first among the signaling pathways enriched to KEGG. Under normal conditions, β-catenin and its corresponding destruction complex

interact and coexist in the cytoplasm, and β-catenin is expressed at a low level.[54] The equilibrium between β-catenin and the destruction complex can be disrupted by activation of this pathway, which promotes the expression of downstream osteogenesis-associated transcription factors, including *RUNX2* and *OPN*.[55] We conjecture that GO has an effect on multiple osteogenesis-related pathways but mainly affects the expression of osteogenesis-related genes through activation of the Wnt/β-catenin pathway. Finally, the results of western blotting and TEC/LEF1 assay verified the cumulative effect of GO on β-catenin as well as on TEC/LEF1 activation.

The present study verified that the AGHP@AMVs composite scaffolds could effectively exert multifunctional antimicrobial, immunomodulatory, and osteogenic properties at the cytological level as well as in the rabbit proximal tibia-infected bone defect model. Future studies will focus on technical optimization to match the degradation rate of the scaffolds as closely as possible to the rate of bone regeneration and to deeply investigate the interaction between GO and cells. Finally, the observation time of implants *in vivo* will be extended to ensure the safe application of inorganic materials *in vivo* and to provide data support for future translational clinical applications.

4. Conclusion

AGHP@AMVs scaffolds have been shown to exert favorable broad-spectrum antimicrobial effects. In addition, it creates favorable conditions for bone regeneration in later stages by remodeling the immune environment. Furthermore, RNA sequencing results elucidated that GO was able to promote osteogenic differentiation of MSCs by activating the Wnt/β-catenin signaling pathway. In conclusion, the composite scaffold has multi-effect properties of antimicrobial activity, immunomodulation, and osteogenesis and is a favorable printable, safe, and effective bone tissue replacement material. Its potential use in the sequential treatment of infected bone defects was also demonstrated.

5. Methods

Material component concentration design: MSCs (Cyagen, Guangzhou, China) from C57BL/6 mice were inoculated at a density of 5×10^3 in 96-well plates and cultured in α-MEM complete medium. Every other day, 0.1, 1, 10, and 100 μg/mL of GO solution (Aladdin, Shanghai, China) was added to

the 96-well plates, and AgNPs solution (Aladdin, Shanghai, China) was also assayed at this concentration gradient. Cell viability was detected on 1, 4, and 7 d of culture using CCK8. Cell viability was assayed in the same manner by combining the AgNPs solution at 0.5, 1, and 10 μg/mL with the GO solution two by two in a concentration gradient of 0.1, 0.5, and 1 μg/mL. LB medium was prepared and *S. aureus* (ATCC6538, USA) was resuscitated. Tryptone 10 g/L, yeast extract 5 g/L, and sodium chloride 10 g/L. *S. aureus* was diluted in LB liquid medium and added to conical flasks at a combination of cell viability assay concentrations. The bacterial suspension was incubated at 37 °C while shaking at 150 rpm. One hundred microliters of the solution were aspirated at different time points to determine the absorbance at 600 nm and plot the bacterial growth inhibition curve.

Fabrication of composite scaffolds: Fabrication of pure scaffolds: The first step entails the formulation of a photosensitive resin pre-mixed solution. This pre-mixed solution is comprised of resin monomer PEG200DA (Aladdin, Shanghai, China), 3,3-dimethyl acrylic adhesive (Aladdin, Shanghai, China), and light initiator (Aladdin, Shanghai, China). According to the proportion of printing molding, 30 wt% nHA (Aladdin, Shanghai, China) powder was mixed into the premix of photosensitive resin three times to produce a light curing paste, and AgNPs and GO powder were added to fabricate three different ratio scaffolds (0.2 wt% AgNps@0.02 wt% GO, 0.5 wt% AgNps@0.05 wt% GO, and 1 wt% AgNps@0.1 wt% GO). Two types of scaffolds of Φ5 mm × h5 mm and Φ10 mm × h2 mm were printed using the 3D printer after the designed porosity was 75% and pore size was 600 μm. The three scaffolds were named 0.2AGHP, 0.5AGHP, and 1AGHP, and the scaffolds containing only nHA and polyethylene glycol diacrylate were named HP.

Fabrication of MVs: RAW264.7 cells (Cyagen, Guangzhou, China) were induced to polarize macrophages to the M2 phenotype with 10 ng/mL of interleukin-4 (IL-4) (Beyotime, Shanghai, China), and the cells were collected one week later. Cells were precipitated through centrifugation at 4 °C, 600 rpm for 5 min. Cell membrane fragments were prepared according to the instructions provided with the Membrane Protein Extraction Kit (Beyotime, Shanghai, China). Finally, the MVs were prepared using a liposome extruder. The MVs used in the animal *in vivo* experiments were prepared in the same manner by inducing rabbit bone marrow macrophages (Immocell, Xiamen, China) with rabbit IL-4 (Qcheng, Shanghai, China) for 1 week.

Assembly of composite scaffolds: Sodium alginate powder (Aladdin, Shanghai, China) was dissolved in pure water to prepare a 40 mg/mL sodium alginate solution and placed on a magnetic stirrer for thorough mixing. The prepared MVs and scaffolds were placed in a sodium alginate solution, and 20 mg/mL $CaCl_2$ solution was added dropwise to crosslink them. After replacing the $CaCl_2$ solution with a new one, the scaffolds were placed in a refrigerator at 4 °C overnight for further cross-linking. The scaffolds were washed with pure water on alternate days to remove the residual calcium ions, and the hydrogel on the surface of the scaffolds retained only the inner hydrogel. The assembled scaffolds were named HP@AMVs and AGHP@AMVs.

Characterization of composite scaffolds: The surface morphology and microstructure of the scaffolds and sodium alginate hydrogels were studied using an SEM (Hitachi S-4800, Japan) equipped with an energy dispersive spectrometer. The morphology of the MVs was observed using TEM (Tecnai G2 F20 S-TWIN, FEI). A laser particle sizer (Zetasizer Nano ZS90, England) was used to detect the particle size of MVs, and the data were analyzed using Zetasizer software. Flow cytometry was used to observe the prepared MVs by detecting the macrophage M2 phenotypic surface markers *CD163* (111803, BioLegend, CA, USA) and *CD206* (141703, BioLegend, CA, USA). In addition, the composite hydrogels were prepared after labeling the MVs with 3,3'-dioctadecyloxacarbocyanine perchlorate and analyzed under a laser scanning confocal microscope (LSCM, LSM 800, ZEISS, Germany) to observe the loading of MVs in the hydrogels. The compressive properties of the samples were evaluated using a universal mechanical testing machine. The standard used was ISO13314:2011 (E). Standard samples (Φ5 mm × h5 mm) were printed with a loading rate of 1 mm/min and the loading direction was along the axis of the cylindrical samples. Tris(hydroxymethyl) aminomethane hydrochloride (Tris-HCl) buffer (pH 5.5 and 7.4) was used to study the solubility, simulated MVs release, and ionic release from sodium alginate hydrogels. The extracts were collected at 37 °C and 150 rpm for 1, 4, 7, and 14 d for each group. The concentration of silver ions in the solution was determined using inductively coupled plasma-mass spectrometry (Agilent, Santa Clara, CA, USA). A certain amount of hydrogel was taken for the first weighing on an analytical balance recorded as S_0, and the hydrogel was placed in Tris-HCl buffer of different pH at 37 °C to fully dissolve, and then the sample was taken out at the set time point, and after sucking away the excess water from the outside of the gel, the hydrogel was weighed for the second time with an analytical balance and recorded as S_t and calculated by the following Equation (1):

$$SR = \frac{S_t}{S_0} \times 100\% \quad (1)$$

Where S_0 is the initial weight of the hydrogel and S_t is the weight of the hydrogel after dissolution at the set point.

The BCA was used to simulate the encapsulation rate and release properties of the MVs. The encapsulation rate of the hydrogels was measured by calculating the ratio (w/w) of the total bovine serum albumin content in the hydrogels to the bovine serum albumin content used in the initial fabrication of the hydrogels. In addition, the prepared bovine serum albumin hydrogel block was placed in 5 mL of Tris-HCL buffer of different pH, and at set time points, 500 µL was aspirated to record its absorbance at 562 nm. Then, the amount of the drug at a certain time point was calculated based on the BCA standard curve. The cumulative release was calculated using Equation (2):

$$Cumulative\ release\ (\%) = \frac{V_e \sum_{i=1}^{n-1} C_i + V_0 C_n}{W_0} \times 100\% \quad (2)$$

Where V_e is the volume of the test release solution (500 µL) taken out each time, W_0 is the total drug content, V_0 is the mediator volume, and C_n is the concentration at the n time point release.

Biocompatibility of composite scaffolds: MSCs from C57BL/6 mice were inoculated in 24-well plates at a density of 1 × 10^4/well, and the composite scaffolds were placed in transwell chambers for indirect co-cultivation with the cells and placed in a humidified incubator at 37 °C with 5% CO_2 to be supplemented with α-MEM complete with 10% fetal bovine serum, 100 mg/mL streptomycin, and 100 U/mL penicillin. Cytotoxicity was detected using CCK8 reagent (Beyotime, Shanghai, China). The effect of the composite scaffolds on cell viability was further detected in the same cell culture using a Live/dead Cell Kit (Beyotime, Shanghai, China) and a Ghost Pen Cyclic Peptide Kit (Beyotime, Shanghai, China). The cells were stained with 500 µL of a combination dye of live/dead staining reagent for 20 min at the time points of 3 and 7 d of culture and then observed under a fluorescence microscope. At the same time points, after fixation with 4% paraformaldehyde, the cells were treated with 0.1% (v/v) Triton X-100 for 15 min, washed again with phosphate-buffered saline (PBS), and labeled with 0.2 mL of Actin-Tracker Red-594 and 0.2 mL of 4,6-diamidino-2-phenylindole (DAPI)

(Beyotime, Shanghai, China) to label actin and nuclei, respectively. Finally, the labeled cells were detected using laser scanning confocal microscopy (LSM 800, ZEISS, Germany). Blood compatibility of the scaffolds was tested using a hemolysis assay. Briefly, each group of scaffolds was individually placed in a centrifuge tube and stabilized by adding 3 mL of PBS for 15 min. PBS (2.5 mL) was added to 2 mL of rabbit blood. Two new centrifuge tubes were used, and 3 mL of water and 3 mL of PBS were added as the positive control (pc) and negative control (nc), respectively. Then, 100 μL of diluted blood was added to all centrifuge tubes and incubated in an incubator at 37 °C for 1 h and centrifuged at 5000 rpm for 3 min. Absorbance at 545 nm was measured using an enzyme meter. The hemolysis rate (HR) was calculated using Equation (3):

$$HR(\%) = \frac{OD_{ts} - OD_{nc}}{OD_{pc} - OD_{nc}} \times 100\% \quad (3)$$

The optical density (OD) data from the test samples (ts), positive control (pc), and negative control (nc) are expressed as OD_{ts}, OD_{pc} and OD_{nc}, respectively.

In vitro broad-spectrum antibacterial and antimicrobial mechanisms: The broad-spectrum antibacterial properties of the composite scaffolds were investigated using the agar plate counting method, dynamic bacterial proliferation, and live/dead bacterial staining, with *E. coli* (BL21, China) and *S. aureus* (ATCC6538, USA) as models. Briefly, the two bacteria were separately resuscitated by LB medium (10 g/L tryptone, 5 g/L yeast extract, and 10 g/L sodium chloride) in a shaker at 37 °C and 150 rpm. The bacterial suspensions (1 mL, 1×10^9 CFU/mL) were mixed with each scaffold group in centrifuge tubes. The surviving bacterial suspension was then diluted 10^6 fold with PBS and spread onto LB plates (1.5% agar), which were incubated at 37 °C for 24 h, and the colonies were photographed and counted. In addition, the two recovered bacteria were diluted with the LB liquid medium to which each group of scaffolds was added. The bacterial suspensions were incubated in a shaker at 37 °C and 150 rpm. Then, 100 μL of bacterial suspensions were extracted at different time points to determine the optical density (OD) values using an enzyme labeler at 600 nm. Finally, the antimicrobial properties of the scaffolds were evaluated using a Bacterial Viability/Toxicity Assay Kit (Solarbio, Beijing, China), and the stained bacteria were detected using a laser scanning confocal microscope (LSM 800, ZEISS, Germany).

The effect of the composite scaffold on the membrane potential of the bacterial surface was determined by measuring zeta potential. *S. aureus* and *E. coli* were resuscitated and cultured to the logarithmic growth stage. An equal volume of bacterial solution was added to each group of scaffolds separately and incubated at 37 °C in an incubator for 1 h. The bacterial fluid was collected, centrifuged, and diluted with PBS to a density of approximately 1×10^8 CFU/mL. For each group, 1 ml of the bacterial fluid was collected and centrifuged. To mimic an acidic environment at the time of infection, the bacteria were resuspended in Tris-HCl buffer at pH 5.5. The membrane potential was detected using a Zetasizer Nano ZS analyzer (Malvern Instruments Ltd, Malvern, United Kingdom).

A ROS assay was used to further explore the antibacterial mechanism of the composite scaffolds. Briefly, *S. aureus* and *E. coli* were resuspended during the logarithmic growth period. An equal volume of bacterial solution was added to each group of scaffolds separately and incubated at 37 °C in an incubator for 1 h. The bacterial solution was collected through centrifugation and diluted with PBS to a density of approximately 1×10^8 CFU/mL. For each group, 1 ml of the bacterial solution was centrifuged. Working solutions were prepared using a Bacterial ROS Assay Kit (Biorab, HR9066, Beijing, China). Then, staining solution (1 ml) was added to each group separately and incubated for 30 min at 37 °C in the dark. The cells were then centrifuged, washed with PBS, and resuspended. The absorbance at excitation and emission wavelengths of 488 and 526 nm, respectively, was detected using an enzyme marker.

Transwell and flow cytometry assay: Transwell migration assay and flow cytometry were used to study the effects of the composite scaffolds on macrophage polarization. The scaffolds were incubated with 700 µL of complete medium containing 10 µg/mL lipopolysaccharides (LPS) and placed in the lower chamber. Then, 2×10^4 MSC cells were suspended with 200 µl of fetal bovine serum-free medium and added to the upper chamber of a 24-well Transwell. After 24 h, the smaller chamber was fixed with 4% paraformaldehyde for 30 min at room temperature, and the cells were removed from the upper surface by scraping. Migrated cells were stained with 0.01% (w/v) crystal violet and photographed under a light microscope (BX 51, Olympus, Japan). Cells located in five random fields in each group were counted using ImageJ software. In addition, RAW264.7 cells were collected after 3 and 7 d of treatment with LPS and scaffolds and stained with the following fluorescently labeled antibodies: *CD163* (BioLegend, 111803, CA, USA) and *CD206* (BioLegend,

141703, CA, USA) incubating in the dark for 30 min. The cells were then analyzed using a flow cytometer (Beckman Coulter, USA).

In vitro osteogenic staining: ALP and ARS staining was performed using 24-well transwell plates with α-MEM medium supplemented with 10% fetal bovine serum, 1% penicillin/streptomycin, 10 nm dexamethasone, 10 mm β-glycerophosphate, and 50 mg/mL ascorbic acid as osteogenic induction medium. MSCs were inoculated into well plates at a density of 2×10^4 cells/well, and the scaffolds were placed in transwells for indirect co-culture. ALP (Beyotime, Shanghai, China) staining solution was added to each well after 7 and 14 d of induction and photographed under a light microscope (BX 51, Olympus, Japan). The cells in each group after 7 and 14 d of induction were collected, lysed, and stained. Then, the solution (100 μL) was placed in a 96-well plate to determine the OD value at 405 nm. Cells were cultured in the same manner and incubated for 30 min by adding ARS (Beyotime, Shanghai, China) staining solution to each well at 14 and 21 d time points, washed, and photographed under a light microscope (BX 51, Olympus, Japan). All samples were eluted in aqueous cetylpyridinium chloride, and the corresponding OD values were measured at 567 nm.

Quantitative real-time polymerase chain reaction (qRT-PCR) and western blot assay: Total RNA was extracted from MSC and RAW 264.7 cells with TRIzol. Relative RNA expression levels were evaluated using qRT-PCR, and the housekeeping gene β-actin was used as an up-sampling control. All qPCR amplifications were performed in the final reaction mixture (20 μL), and the relevant primer sequences are shown in Table S1, Supporting Information. Forty cycles of amplification reactions were performed using Hieff qPCR SYBR Green Master Mix (Yeason, 11201 ES 03, China), and relative expression was calculated according to the $2^{-\Delta\Delta Ct}$ method.

Total protein was extracted from MSC and RAW 264.7 cells, lysed using radioimmunoprecipitation assay, and protein concentration was determined using a Bicinchoninic Acid Assay Kit (Beyotime, Shanghai, China). Equal amounts of protein were electrophoresed using sodium dodecyl sulfate-polyacrylamide gel electrophoresis and transferred onto pure nitrocellulose blotting membranes. They were blocked with 5% (w/v) skimmed milk powder for 1 h at room temperature and then incubated with primary antibodies against β-catenin (1:1000, 4970, CST), β-actin (1:1000, 9582, CST), H3 (1:2000, 4499, CST), TNFα (1:1000, 3707, CST), STAT3 (1:1000, 30835, CST), p-STAT3

(1:2000, 9145, CST), mTOR (1:1000, 2972, CST), IκBα (1:1000, 9242, CST), and RelA (1:1000, 8242, CST) at 4 °C overnight. The membrane was washed three times with Tris-buffered saline and incubated with a horseradish peroxidase-conjugated secondary antibody (1:10,000) at room temperature for 1 h. The antigen-antibody complexes were quantitatively analyzed using ImageJ software after detection using an enhanced chemiluminescence system.

Extraction of nuclear protein and cytoplasmic protein: RAW264.7 cells were treated using a Nuclear and Cytoplasmic Protein Extraction Kit (Beyotime, P0027, China). Briefly, lysis solutions of the cytoplasm and nucleus were used to lyse whole cells sequentially. Distribution and centrifugation were then performed to extract the relevant protein lysates.

Measurement of T-cell factor/lymphoid enhancer factor 1(TEC/LEF1): A TCF/LEF1 Luciferase Reporter Kit (Yeasen, Shanghai, China) was used to measure TEC/LEF1 activation. Refer to the manufacturer's instructions for the specific experimental procedures.

Infected bone defect model construction: All animal experiments were approved by the Ethical Review Committee of the Chongqing Medical University (No. IACUC-CQMU-2023-0182). Thirty New Zealand rabbits (2.5 kg, half male and half female) were provided by the Experimental Animal Center of Chongqing Medical University. The rabbits were anesthetized with 3% (w/v) sodium pentobarbital, and a 3 cm incision was made in the right calf to separate the muscle and fascia and expose the medial tibia. Then, a defect of 5 mm in diameter and 5 mm in depth was created in the proximal end of the medial tibia with a chainsaw. The wounds were cleaned with saline to dissipate the heat generated by the chainsaw. Subsequently, a 5 mm diameter, 5 mm height hexagonal screw with *S. aureus* attachment was implanted, and the wound was closed with a No. 5-0 absorbable suture. Two weeks later, the screws were removed and the wound was sutured directly without implant placement in the Blank group, which served as the control group after debridement. The other groups were sequentially implanted with the cylindrical scaffolds of HP, HP@AMVs, AGHP, and AGHP@AMVs, each with a diameter and height of 5 mm, before the wounds were sutured. Four and eight weeks after surgery, rabbits in all groups were sacrificed using an overdose of sodium

pentobarbital, and whole tibiae were harvested and fixed in 4% (w/v) paraformaldehyde at 4 °C for 48 h for further analysis.

Micro-computed tomography (micro-CT), histologic, and immunohistochemical analysis: A micro-CT imaging system (InspeXio SMX-225 CT FPD HR, Japan) was used for *in vivo* bone formation evaluation. All tibia samples were scanned at an accelerating voltage of 150 kV, a current of 150 μA, and a resolution of 5.4 μm, and a cylindrical region with a diameter of 6 mm and a depth of 6 mm was used as the volume of interest. All data were analyzed using VG Studio MAX software (Volume Graphics, Germany), and the reconstructive parameters used to assess new bone formation mainly included BMD, BV/TV, Tb. Sp, and Tb. N.

Tibial samples were immersed in ethylenediaminetetraacetic acid (pH 7.2) and placed on a shaker for four weeks before paraffin embedding. Areas of bone defects containing scaffolds were cut, and paraffin sections with a thickness of 4 μm were prepared. The bone repair capacity was qualitatively evaluated using HE and Masson staining. Gram staining was used to evaluate the antimicrobial effects *in vivo*. *iNOS* (1:300, bs-2072R, Bioss) and *CD206* (1:300, S1-A48959, Chongqing Sailuo Hezhi Biological Technology Co., LTD) antibodies were used for immunohistochemical staining. Further analysis of the immunomodulatory effect was performed using ImageJ software. Sections were scanned and analyzed using a KF-PRO-120/FL scanner (Olympus, Japan).

Transcriptome sequencing (RNA-seq) data analysis: The HP group was used as the control group, and the AGHP@AMVs group was used as the experimental group (3 *vs*. 3) to treat RAW264.7 and MSC cells, respectively. The specific procedures were as follows: indirect co-culture of scaffolds and cells was conducted using 24-well transwell plates, and the well plates were inoculated with RAW264.7 cells as well as MSC cells; RAW264.7 cells were cultured in LPS medium containing 10 μg/mL for 3 and 7 d, and MSC cells were cultured in an osteogenic induction culture for 10 d, and scaffolds were placed in the chambers. RAW264.7 and MSCs at each time point were collected, and total RNA was extracted. Sequencing was performed by Cell Networks (Heidelberg, Germany) on an Illumina HiSeq platform. Sequencing reads were aligned to the mouse reference genome using the TopHat 2 software (version 2.0.1.14). The top 10 genes associated with macrophage polarization and osteogenesis were screened and analyzed for Gene Ontology and Kyoto Encyclopedia of Genes and

Genomes (KEGG) enrichment. The fold-change (FC) between the control and experimental samples was used to define genes that were upregulated (FC > 1.5), unchanged (0.667 < FC < 1.5), or downregulated (FC < 0.667). Heatmaps and bubble plots were drawn using Sangerbox (version 3.0) to show changes in macrophage polarization status, osteogenesis-related genes, and signaling pathways in the experimental groups from the relevant RNA-seq datasets.

Statistical analysis: All data from each trial were collected from at least three parallel samples and expressed as mean ± SD. Statistical analyses were performed using GraphPad Prism software (v6.0a; La Jolla, CA, USA). Unpaired Student's t-tests were used for two-group comparisons, and one-way analysis of variance (ANOVA) with Tukey's post-hoc test was used for three-group comparisons. Statistical significance was set at $P < 0.05$. *$P < 0.05$, **$P < 0.01$, and ***$P < 0.001$.

Acknowledgements

This work was supported by National Natural Science Foundation of China (3227090327), the National Natural Science Foundation of China (82102610), Chongqing Natural Science Foundation Key Project (CSTB2023NSCQ-LZX0018), Youth Talent Support Program of the First Affiliated Hospital of Chongqing Medical University (BJRC2021-02), and the Science and Technology Research Project of Chongqing Education Commission (KJQN202200404).

Conflict of Interest

The authors declare no conflict of interest.

Author Contributions

M.S. and Y.L. contributed equally to this work. M.S. and J.Z. conceived the project. M.S. designed the experiments. M.S., Y.L., H.Z., W.J., W.W., S.Z., X.H., D.X., B.T., and Y.C. performed the experiments. M.S. and Y.L. interpreted the data. M.S. wrote the manuscript. T.C., C.L. and J.Z. reviewed and edited the manuscript. All authors read and approved the final manuscript.

Data Availability Statement

The data that support the findings of this study are available from the corresponding author upon reasonable request.

References

[1] X. Cui, Y. Zhang, J. Wang, C. Huang, Y. Wang, H. Yang, W. Liu, T. Wang, D. Wang, G. Wang, C. Ruan, D. Chen, W. W. Lu, W. Huang, M. N. Rahaman, H. Pan, Bioact. Mater. 2020, 5, 334.

[2] P. Jungbluth, L. S. Spitzhorn, J. Grassmann, S. Tanner, D. Latz, M. S. Rahman, M. Bohndorf, W. Wruck, M. Sager, V. Grotheer, P. Kropil, M. Hakimi, J. Windolf, J. Schneppendahl, J. Adjaye, Bone Res. 2019, 7, 32.

[3] Y. X. Ma, K. Jiao, Q. Q. Wan, J. Li, M. Y. Liu, Z. B. Zhang, W. Qin, K. Y. Wang, Y. Z. Wang, F. R. Tay, L. N. Niu, Bioact. Mater. 2022, 9, 475.

[4] J. Gu, Q. Zhang, M. Geng, W. Wang, J. Yang, A. U. R. Khan, H. Du, Z. Sha, X. Zhou, C. He, Bioact. Mater. 2021, 6, 3254.

[5] W. Zhu, K. R. Tringale, S. A. Woller, S. You, S. Johnson, H. Shen, J. Schimelman, M. Whitney, J. Steinauer, W. Xu, T. L. Yaksh, Q. T. Nguyen, S. Chen, Mater. Today (Kidlington) 2018, 21, 951.

[6] C. Garot, G. Bettega, C. Picart, Adv. Funct. Mater. 2021, 31.

[7] C. Chen, L. Cheng, M. D. Weir, N. J. Lin, S. Lin-Gibson, X. D. Zhou, H. H. Xu, Int. J. Oral Sci. 2016, 8, 239.

[8] J. Wu, F. Li, X. Hu, J. Lu, X. Sun, J. Gao, D. Ling, ACS Cent. Sci. 2019, 5, 1366.

[9] A. Vanangamudi, S. Hamzah, G. Singh, Chem. Eng. J. 2015, 260, 801.

[10] H. Singh, J. Du, P. Singh, T. H. Yi, J. Pharm. Anal. 2018, 8, 258.

[11] M. M. Hossein, S. A. Potash, M. Takikawa, R. D. Shubhra, T. Saha, Z. Islam, S. Hossein, M. A. Hasan, S. Takeoka, S. R. Sarker, Front. Bioeng. Biotechnol. 2019, 7.

[12] A. Baran, M. Firat Baran, C. Keskin, A. Hatipoglu, O. Yavuz, S. Irtegun Kandemir, M. T. Adican, R. Khalilov, A. Mammadova, E. Ahmadian, G. Rosic, D. Selakovic, A. Eftekhari, Front. Bioeng. Biotechnol. 2022, 10.

[13] P. Khandel, S. K. Shahi, D. K. Soni, R. K. Yadaw, L. Kanwar, Nano Converg. 2018, 5.

[14] H. Yazdani-Ahmadabadi, D. F. Felix, K. Yu, H. H. Yeh, H. D. Luo, S. Khoddami, L. E. Takeuchi, A. Alzahrani, S. Abbina, Y. Mei, L. Fazli, D. Grecov, D. Lange, J. N. Kizhakkedathu, ACS Cent. Sci. 2022, 8, 546.

[15] A. Agarwal, K. M. Guthrie, C. J. Czuprynski, M. J. Schurr, J. F. McAnulty, C. J. Murphy, N. L. Abbott, Adv. Funct. Mater. 2011, 21, 1863.

[16] J. Neves, J. Zhu, P. Sousa-Victor, M. Konjikusic, R. Riley, S. Chew, Y. Qi, H. Jasper, D. A. Lamba, Science 2016, 353.

[17] W. Wang, T. Li, X. Wang, W. Yuan, Y. Cheng, H. Zhang, E. Xu, Y. Zhang, S. Shi, D. Ma, W. Han, Cell. Mol. Immunol. 2015, 12, 615.

[18] A. Liu, S. Jin, C. Fu, S. Cui, T. Zhang, L. Zhu, Y. Wang, S. G. F. Shen, N. Jiang, Y. Liu, Int. J. Oral Sci. 2020, 12.

[19] W. Kim, S. K. Khan, Y. Liu, R. Xu, O. Park, Y. He, B. Cha, B. Gao, Y. Yang, Gut 2018, 67, 1692.

[20] J. Lv, Z. Wang, Y. Qu, H. Zhu, Q. Zhu, W. Tong, L. Bao, Q. Lv, J. Cong, D. Li, W. Deng, P. Yu, J. Song, W.-M. Tong, J. Liu, Y. Liu, C. Qin, B. Huang, Cell Discov. 2021, 7.

[21] L. Zhong, D. Liao, J. Li, W. Liu, J. Wang, C. Zeng, X. Wang, Z. Cao, R. Zhang, M. Li, K. Jiang, Y.-X. Zeng, J. Sui, T. Kang, Signal Transduct. Target. Ther. 2021, 6.

[22] B. Zhang, F. Han, Y. Wang, Y. Sun, M. Zhang, X. Yu, C. Qin, H. Zhang, C. Wu, Adv. Sci. (Weinh) 2022, 9.

[23] Z. Lin, D. Shen, W. Zhou, Y. Zheng, T. Kong, X. Liu, S. Wu, P. K. Chu, Y. Zhao, J. Wu, K. M. C. Cheung, K. W. K. Yeung, Bioact. Mater. 2021, 6, 2315.

[24] R. K. Radhakrishnan, R. S. Thandi, D. Tripathi, P. Paidipally, M. K. McAllister, S. Mulik, B. Samten, R. Vankayalapati, JCI insight 2020, 5.

[25] D. Patoli, F. Mignotte, V. Deckert, A. Dusuel, A. Dumont, A. Rieu, A. Jalil, K. Van Dongen, T. Bourgeois, T. Gautier, C. Magnani, N. Le Guern, S. Mandard, J. Bastin, F. Djouadi, C. Schaeffer, N. Guillaumot, M. Narce, M. Nguyen, J. Guy, A. Dargent, J.-P. Quenot, M. Rialland, D. Masson, J. Auwerx, L. Lagrost, C. Thomas, J. Clin. Invest. 2020, 130, 5858.

[26] H.-L. Gao, R. Zhao, C. Cui, Y.-B. Zhu, S.-M. Chen, Z. Pan, Y.-F. Meng, S.-M. Wen, C. Liu, H.-A. Wu, S.-H. Yu, Natl. Sci. Rev. 2020, 7, 73.

[27] X. Zhang, Y. Li, Z. Ma, D. He, H. Li, Bioact. Mater. 2021, 6, 3692.

[28] J.-N. Ma, Y.-L. Zhang, D.-D. Han, J.-W. Mao, Z.-D. Chen, H.-B. Sun, Natl. Sci. Rev. 2020, 7, 775.

[29] G. Gao, H. B. Wu, B. Dong, S. Ding, X. W. Lou, Adv. Sci. (Weinh) 2015, 2.

[30] C.-N. Yeh, H. Huang, A. T. O. Lim, R.-H. Jhang, C.-H. Chen, J. Huang, Nat. Commun. 2019, 10.

[31] S. K. Tuteja, C. Ormsby, S. Neethirajan, Nanomicro Lett. 2018, 10.

[32] Z. Zhang, S. Gao, Y.-N. Hu, X. Chen, C. Cheng, X.-L. Fu, S.-S. Zhang, X.-L. Wang, Y.-W. Che, C. Zhang, R.-J. Chai, Adv. Sci. (Weinh) 2022, 9.

[33] E. Sayin, R. H. Rashid, J. Carlos Rodriguez-Cabello, A. Elsheikh, E. T. Baran, V. Hasirci, Bioact. Mater. 2017, 2, 71.

[34] B. Jia, H. Yang, Z. Zhang, X. Qu, X. Jia, Q. Wu, Y. Han, Y. Zheng, K. Dai, Bioact. Mater. 2021, 6, 1588.

[35] T. Russo, A. Gloria, R. De Santis, U. D'Amora, G. Balato, A. Vollaro, O. Oliviero, G. Improta, M. Triassi, L. Ambrosio, Bioact. Mater. 2017, 2, 156.

[36] J. M. Song, S. H. Shin, Y. D. Kim, J. Y. Lee, Y. J. Baek, S. Y. Yoon, H. S. Kim, Int. J. Oral Sci. 2014, 6, 87.

[37] A. Hoppe, N. S. Gueldal, A. R. Boccaccini, Biomaterials 2011, 32, 2757.

[38] Y. Qian, J. Song, X. Zhao, W. Chen, Y. Ouyang, W. Yuan, C. Fan, Adv. Sci. (Weinh) 2018, 5.

[39] Q. Dong, D. Zu, L. Kong, S. Chen, J. Yao, J. Lin, L. Lu, B. Wu, B. Fang, Biomater. Res. 2022, 26.

[40] Z. Li, S. Xiang, Z. Lin, E. N. Li, H. Yagi, L. Yocum, L. Li, K. K. Bruce, M. R. Fritch, H. Hu, B. Wang, P. G. Alexander, K. A. Khor, R. S. Tuan, H. Lin, Biomaterials 2021, 277.

[41] L. A. Genova, M. F. Roberts, Y.-C. Wong, C. E. Harper, A. G. Santiago, B. Fu, A. Srivastava, W. Jung, L. M. Wang, L. Krzeminski, X. Mao, X. Sun, C.-Y. Hui, P. Chen, C. J. Hernandez, Proc. Natl. Acad. Sci. U. S. A. 2019, 116, 25462.

[42] S. Ruiz, J. Andres Tamayo, J. Delgado Ospina, D. P. Navia Porras, M. E. Valencia Zapata, J. H. Mina Hernandez, C. Humberto Valencia, F. Zuluaga, C. D. Grande Tovar, Biomolecules 2019, 9.

[43] K. C. L. Black, T. S. Sileika, J. Yi, R. Zhang, J. G. Rivera, P. B. Messersmith, Small 2014, 10, 169.

[44] M.-m. Lu, Q.-j. Wang, Z.-m. Chang, Z. Wang, X. Zheng, D. Shao, W.-f. Dong, Y.-m. Zhou, Int. J. Nanomedicine 2017, 12, 3577.

[45] A. Moshaverinia, C. Chen, X. Xu, S. Ansari, H. H. Zadeh, S. R. Schricker, M. L. Paine, J. Moradian-Oldak, A. Khademhosseini, M. L. Snead, S. Shi, Adv. Funct. Mater. 2015, 25, 2296.

[46] L. Yan, L. Wang, J. Wu, Y. Wu, X. Zhu, Q. Mei, Y. Song, Y. Liu, L. Zhang, J. Ai, K. Li, G. Qing, Y. Zhang, X. Xiao, Y. Zhao, W. Xiang, NPJ Regen. Med. 2022, 7.

[47] S. Zhu, C. Yu, N. Liu, M. Zhao, Z. Chen, J. Liu, G. Li, H. Huang, H. Guo, T. Sun, J. Chen, J. Zhuang, P. Zhu, Bioact. Mater. 2022, 13, 119.

[48] M. Taale, F. Schuett, T. Carey, J. Marx, Y. K. Mishra, N. Stock, B. Fiedler, F. Torrisi, R. Adelung, C. Selhuber-Unkel, ACS App.l Mater. Interfaces 2019, 11, 5325.

[49] Y. He, R. M. Rodrigues, X. Wang, W. Seo, J. Ma, S. Hwang, Y. Fu, E. Trojnar, C. Matyas, S. Zhao, R. Ren, D. Feng, P. Pacher, G. Kunos, B. Gao, J. Clin. Invest. 2021, 131.

[50] J. Hu, Y. Ding, B. Tao, Z. Yuan, Y. Yang, K. Xu, X. Li, P. Liu, K. Cai, Bioact. Mater. 2022, 18, 228.

[51] J. Liu, Y. Pang, S. Zhang, C. Cleveland, X. Yin, L. Booth, J. Lin, Y.-A. L. Lee, H. Mazdiyasni, S. Saxton, A. R. Kirtane, T. von Erlach, J. Rogner, R. Langer, G. Traverso, Nat. Commun. 2017, 8.

[52] L. Chen, D. Wang, J. Qiu, X. Zhang, X. Liu, Y. Qiao, X. Liu, Bioact. Mater. 2021, 6, 191.

[53] D. Jiao, J. Wang, W. Yu, K. Zhang, N. Zhang, L. Cao, X. Jiang, Y. Bai, Bioact. Mater. 2022, 15, 409.

[54] D. Kimelman, W. Xu, Oncogene 2006, 25, 7482.

[55] H. Jin, B. Wang, J. Li, W. Xie, Q. Mao, S. Li, F. Dong, Y. Sun, H.-Z. Ke, P. Babij, P. Tong, D. Chen, Bone 2015, 71, 63.

ToC:

This study successfully fabricated a multifunctional integrated composite scaffold using 3D printing technology, which encompasses nano-silver, graphene oxide, and macrophage membrane vesicles. This composite scaffold demonstrated excellent antibacterial, immunomodulatory, and osteogenic properties, and exhibited favorable biocompatibility *in vivo*. This provides a potential strategy for the sequential treatment of infected bone defects.

ToC figure: